Reconstruction of Voronoi diagrams
in inverse potential problems*

Ernesto G. Birgin†   Antoine Laurain‡   Danilo R. Souza§

April 18, 2024

Abstract

In this paper we propose and analyze a numerical method for the recovery of a piecewise constant parameter with multiple phases in the inverse potential problem. The potential is assumed to be constant in each phase, and the phases are modeled by a Voronoi diagram generated by a set of sites, which are used as control parameters. We first reformulate the inverse problem as an optimization problem with respect to the position of the sites. Combining techniques of non-smooth shape calculus and sensitivity of Voronoi diagrams, we are able to compute the gradient of the cost function, under standard non-degeneracy conditions of the diagram. We provide two different formulas for the gradient, a volumetric and an interface one, which are compared in numerical experiments. We provide several numerical experiments to investigate the dependence of the reconstruction on the problem parameters, such as noise, number of sites and initialization.

Keywords: Inverse potential problem, non-smooth shape calculus, Voronoi diagrams, optimization.

AMS subject classifications: 49Q10, 49J52, 49Q12.

1   Introduction

In this paper we study the inverse problem of recovering a potential $q \in L^\infty(\mathcal{D})$, $q > 0$, $\mathcal{D} \in \mathbb{R}^2$, from observations h_α in $\mathcal{D}$ that are noisy perturbations of the exact data $u_\alpha^\star$, solution of

$$-\Delta u_\alpha^\star + q\, u_\alpha^\star = f_\alpha \text{ in } \mathcal{D}, \tag{1}$$
$$u_\alpha^\star = 0 \text{ on } \partial\mathcal{D}, \tag{2}$$

and f_α are known sources. We are interested in the case where q is piecewise constant with complex, non-smooth interfaces between the different regions and we model the phases using a Voronoi diagram, which provides a natural and simple way to obtain a finite-dimensional parameterization of non-smooth shapes.

The inverse potential problem arises in several applications such as quantitative dynamic elastography [21] or the reconstruction of the heat radiative coefficient [20, 50]. The convergence rates for Tikhonov regularization of the problem of identifying q were investigated in [27], and also in [23] in the one-dimensional elliptic case. Conditional stability estimates and an error analysis of a reconstruction scheme based on the output least-squares formulation with Tikhonov regularization have been obtained in [33]. Lipschitz stability estimates have also been obtained for a similar problem with piecewise constant potential on an unknown tetrahedral partition in [8], for recovering the wavespeed in the Helmholtz

†Department of Computer Science, Institute of Mathematics and Statistics, University of São Paulo, Rua do Matão, 1010, Cidade Universitária, 05508-090, São Paulo, SP, Brazil. e-mail: egbirgin@ime.usp.br. Corresponding author.

‡Faculty of Mathematics, University of Duisburg-Essen, Thea-Leymann-Str. 9, 45127, Essen, Germany, e-mail: antoine.laurain@uni-due.de

§Department of Applied Mathematics, Institute of Mathematics and Statistics, University of São Paulo, Rua do Matão, 1010, Cidade Universitária, 05508-090, São Paulo, SP, Brazil. e-mail: danilogyn01@gmail.com

equation. The inverse problem of recovering q in the parabolic case has also been investigated in the literature, see for instance [7, 20, 34, 50]. The inverse problem of gravimetry, which corresponds roughly speaking to the recovering of f_α in (1), is also sometimes called inverse potential problem, see [18, 19, 30] for the piecewise constant case.

A large part of the literature on numerical methods for inverse problems focuses on the reconstructions of relatively smooth functions, or at least continuous functions. Nonetheless, it is equally crucial to address the recovery of discontinuous functions and sharp interfaces, especially given their significance in various applications such as geophysics, civil engineering, and medicine. Several types of methods have been developed to tackle such cases, such as total variation schemes [5], the enclosure method [29], the MUSIC algorithm for small inclusions [3], monotonicity-based shape reconstructions [28] and topological derivative-based methods [2, 19, 31]. Shape optimization methods have been employed, using level set methods [1, 39], and the non-smooth case has also been considered in electrical impedance tomography for the reconstruction of polygons [9].

In this work we focus on the case where the potential q to be recovered is a piecewise constant function. In this way the problem is then to reconstruct the interfaces delineating the regions where the potential remains constant. Consequently, the problem can be reformulated as a shape optimization problem [22, 39, 46]. In this framework, one often considers a piecewise constant parameter with binary values, and the goal is then to reconstruct the interface, usually smooth, between these two values [3, 39]. The recovery of more than two regions, also referred to as phases, has been considered in inverse problems [42] employing frameworks such as the multiphase level set method introduced in [49] or the more recent moving morphable components method [41]. In our study, we also address a multiphase problem, but we are interested in the specific case where the phases can be parameterized by a finite number of scalar parameters. Consequently, the domain of the potential q can be partitioned into cells such that the potential is constant in each cell. Furthermore, we suppose that the set of cells is given by a Voronoi diagram, a natural and practical setting for a multiphase problem. Previous research has explored inverse problems for oriented Voronoi diagrams, notably in [17], where the Voronoi diagrams model the microstructure of polycrystalline metals. Additionally, the inverse problem of obtaining the Voronoi diagram which approximates a given tessellation of the plane, sometimes called *Inverse Voronoi Problem*, has also been considered in the literature, see [4, 48]. Compared to other approaches such as the multiphase level set framework, our approach presents several interesting features. Firstly, the optimization problem is finite-dimensional, enabling a reduction in the search space. Secondly, it naturally models complex nonsmooth geometric features such as triple points between phases. Thirdly, it permits the inclusion of geometric constraints in the model when relevant, such as enforcing straight interfaces.

The multiphase modeling using Voronoi diagrams poses several significant challenges. In order to compute the gradient of the cost functional, we combine techniques from non-smooth shape calculus [22, 39, 46] and from the sensitivity analysis for Voronoi diagrams [14]. Indeed, the cost functional is a composition of a non-smooth shape function, as it depends on the cells shapes, with the function parameterizing the cells. For the non-smooth shape calculus, we rely in particular on the notion of distributed shape derivative and its tensor representation, see [38, 39]. Indeed, this allows us to work with low-regularity shapes, which is appropriate in the context of Voronoi diagrams, where the cells are polygons. Compared to previous work on non-smooth, parameterized shape optimization, where only the interface representation of the gradient was obtained [11, 13], an important novelty of the present study is to provide two different ways to express the gradient of the cost function, a distributed (volumetric) representation and an interface representation of the gradient. Note that even though the use and usefulness of distributed expressions is now well-established in shape optimization [32, 37, 39], it is a challenging task in non-smooth, parameterized shape optimization which has not been explored yet. For the sensitivity analysis of Voronoi diagrams, we employ a particular case of the theory developed in [14] for minimization diagrams. Compared to [14], a novel aspect and an additional difficulty here is that the problem depends on the solution of a PDE, which requires the use of shape calculus and the study of the regularity of the PDE as well as the tensors involved in the shape gradient.

The paper is organized as follows. We start by describing the mathematical model of the elliptic inverse potential problem in Section 2, as well as the piecewise constant, multiphase hypothesis considered for the potential q in this paper. In Section 3, we describe how to compute derivatives with respect to the sites of cost functionals depending on Voronoi diagrams. We use some elements of the general theory of [14] and apply the tools of shape calculus in the context of multiphase, non-smooth shape optimization. In Section 4, we apply the general results of Section 3 to the particular case of the inverse

potential problem, formulated as an optimization problem, and obtain two different expressions of the gradient of the cost function. In Section 5 we perform several experiments to investigate the dependence of the reconstruction algorithm on the various parameters of the problem. We analyze the influence of several factors on the optimization process, including the number of sites in the Voronoi diagram describing the potential, the distribution of the potential values across the diagram's cells, the initial starting point in the optimization process, the presence of noise in observation data, and the utilization of the two distinct expressions of the gradient. The final section presents conclusions and directions for future work.

2   Mathematical model

We start with a description of the mathematical model. Let $\mathcal{D} \subset \mathbb{R}^2$ be a bounded, Lipschitz, simply connected, and piecewise $\mathcal{C}^1$ domain. For a given ground truth potential $q^\star \in L^\infty(\mathcal{D})$ and a given set of sources $\{f_\alpha\}_{\alpha=1}^{\bar\alpha}$, $f_\alpha \in L^2(\mathcal{D})$, the potential $u_\alpha^\star \in H_0^1(\mathcal{D})$ is the solution to

$$-\Delta u_\alpha^\star + q^\star u_\alpha^\star = f_\alpha \text{ in } \mathcal{D}, \tag{3}$$

$$u_\alpha^\star = 0 \text{ on } \partial\mathcal{D}, \tag{4}$$

where $H_0^1(\mathcal{D}) := \{v \in H^1(\mathcal{D}) : v = 0 \text{ on } \partial\mathcal{D}\}$. The variational formulation of (3)-(4) reads: Find $u_\alpha^\star \in H_0^1(\mathcal{D})$ such that

$$\int_\mathcal{D} \nabla u_\alpha^\star \cdot \nabla v + q^\star u_\alpha^\star v = \int_\mathcal{D} f_\alpha v, \qquad \forall v \in H_0^1(\mathcal{D}). \tag{5}$$

The inverse potential problem consists in reconstructing the ground truth $q^\star$ from the knowledge of a data set $\{f_\alpha, h_\alpha\}_{\alpha=1}^{\bar\alpha}$, where $h_\alpha := u_\alpha^\star + \eta_\alpha$ is a noisy measurement of the potential $u_\alpha^\star$ in $\mathcal{D}$, and $\eta_\alpha : \mathcal{D} \to \mathbb{R}$ is a measurement noise. A standard approach to compute a numerical approximation of the ground truth is to minimize the least-squares cost function

$$J(q) = \frac{1}{2} \sum_{\alpha=1}^{\bar\alpha} \zeta_\alpha \int_\mathcal{D} (u_\alpha(q) - h_\alpha)^2,$$

where the model $u_\alpha = u_\alpha(q)$ satisfies a PDE as (3)-(4), but with the trial potential $q \in L^\infty(\mathcal{D})$ instead of the ground truth $q^\star$, i.e.,

$$-\Delta u_\alpha + q\, u_\alpha = f_\alpha \text{ in } \mathcal{D}, \tag{6}$$

$$u_\alpha = 0 \text{ on } \partial\mathcal{D}. \tag{7}$$

In numerical experiments, the weights $\zeta_\alpha \in \mathbb{R}, \zeta > 0$, are chosen so that the terms in the sum over α have a similar magnitude, in order to obtain a more balanced contribution of each u_α to the cost functional. Since the h_α are noisy measurements, one cannot achieve $u_\alpha(q) = h_\alpha$ exactly, but the distance between $u_\alpha(q)$ and h_α can be minimized by minimizing $J(q)$.

Since the inverse potential problem is ill-posed [33], prior knowledge on the ground truth $q^\star$ can be included in the mathematical model which helps reducing the ill-posedness. In this work we assume that $q^\star$ is piecewise constant, i.e., $q^\star(x) \in \{q_1, q_2, \ldots, q_{\kappa_0}\}$ for all $x \in \mathcal{D}$, where $q_1, q_2, \ldots, q_{\kappa_0}$ are constants. This is a common hypothesis for the modeling of discontinuous functions. In the case where the values $\{q_1, q_2, \ldots, q_{\kappa_0}\}$ are known a priori, the problem then amounts to determining the phases $\Omega_i := \{x \in \mathcal{D} : q^\star(x) = q_i\}$, which can be formulated as a *multiphase shape optimization* problem. For this purpose, let us introduce partitions of $\mathcal{D}$, called diagrams, indexed by a set of indices $\mathcal{K}$.

Definition 1 ($\mathcal{K}$-diagrams of $\mathcal{D}$)**.** *Let $\mathbb{P}$ denote the set of open subsets of $\mathcal{D} \subset \mathbb{R}^2$. For a given finite set of indices $\mathcal{K} \subset \mathbb{N}$, $\mathbb{P}_\mathcal{K}(\mathcal{D})$ denotes the set of $\mathcal{K}$-diagrams $\boldsymbol{\Omega} := \{\Omega_k\}_{k\in\mathcal{K}}$ with $\Omega_k \in \mathbb{P}$ for all $k \in \mathcal{K}$, $\Omega_k \cap \Omega_\ell = \emptyset$ for all $\{k,\ell\} \subset \mathcal{K}, \ k \neq \ell$ and $\bigcup_{k\in\mathcal{K}} \overline{\Omega_k} = \overline{\mathcal{D}}$.*

We also use a piecewise constant trial potential of the form $q_{\boldsymbol{\Omega}} := \sum_{i\in\mathcal{K}} q_i \chi_{\Omega_i}$, where χ_{Ω_i} denotes the characteristic function of Ω_i. Depending on the application, one can assume $\mathcal{K}$ and q_i are either

known or unknown, for all $i \in \mathcal{K}$. Assuming they are known, the cost function becomes the following multiphase function:

$$\mathfrak{J}(\boldsymbol{\Omega}) := J(q_{\boldsymbol{\Omega}}) = \frac{1}{2} \sum_{\alpha=1}^{\bar{\alpha}} \zeta_\alpha \int_{\mathcal{D}} (u_\alpha(q_{\boldsymbol{\Omega}}) - h_\alpha)^2. \tag{8}$$

We also need to consider a parameterization of the diagram $\boldsymbol{\Omega}$ that is tractable both for the analysis and for the numerics. In this work we consider the case where $\boldsymbol{\Omega}$ forms a Voronoi diagram; this allows to model a complex non-smooth geometry using only a few parameters. More complex geometries could also be considered in a similar way, for instance using minimization diagrams and the formulas presented in [14]. Let $\mathcal{K}_{\text{vor}} = \{1, \ldots, \kappa_0\}$ be a set of indices, $\mathbf{a} = \{a_k\}_{k \in \mathcal{K}_{\text{vor}}}$ be a set of points in the plane, named sites, and denote by $\boldsymbol{\Omega}(\mathbf{a}) := \{\Omega_k(\mathbf{a})\}_{k \in \mathcal{K}_{\text{vor}}}$ the Voronoi diagram associated with a set of sites $\mathbf{a}$, where the cells of the diagram are defined by

$$\Omega_i(\mathbf{a}) := \{x \in \mathcal{D} \text{ such that } \|x - a_i\| \le \|x - a_j\| \text{ for all } j \in \mathcal{K}_{\text{vor}} \setminus \{i\}\}.$$

We assume that the ground truth potential $q^\star$ is piecewise constant and the regions where $q^\star$ is constant are cells of a Voronoi diagram associated with the set of sites $\mathbf{a}^\star$, i.e.,

$$q^\star = \sum_{i \in \mathcal{K}_{\text{vor}}} q_i \chi_{\Omega_i(\mathbf{a}^\star)}.$$

Introducing the reduced cost function

$$G(\mathbf{a}) := \mathfrak{J}(\boldsymbol{\Omega}(\mathbf{a})), \tag{9}$$

we have reformulated the inverse problem into the following finite-dimensional unconstrained optimization problem:

$$\underset{\mathbf{a} \in \mathbb{R}^{2\kappa_0}}{\text{Minimize}} \, G(\mathbf{a}). \tag{10}$$

Notation. We use $y^\perp := Ry$, for a vector $y \in \mathbb{R}^2$, where R is a rotation matrix of angle $\pi/2$ with respect to a counterclockwise orientation. The identity matrix in $\mathbb{R}^{2 \times 2}$ is denoted by I_d. We denote by $\mathcal{E}_i^{\text{int}}$ and $\mathcal{V}_i^{\text{int}}$ the sets of interior edges and interior vertices of the cell $\Omega_i(\mathbf{a})$, respectively, i.e., edges and vertices that are included in $\mathcal{D}$. The set $\mathcal{V}_i^{\text{bd}}$ denotes the set of boundary vertices of the cell $\Omega_i(\mathbf{a})$, i.e., vertices of $\Omega_i(\mathbf{a})$ that belong to $\partial \mathcal{D}$ and to another cell $\Omega_j(\mathbf{a})$, $j \ne i$.

3 Sensitivity analysis for Voronoi diagrams involving PDEs

In this section we provide general formulas for computing the gradient of cost functions depending on Voronoi diagrams. For this purpose we combine the theory of multiphase, non-smooth shape calculus [12, 38] and the general theory developed in [14] for the sensitivity analysis with respect to minimization diagrams. Here, we face an additional layer of difficulty compared to [14], as the cost functional also depends on a PDE. The notion of distributed shape derivative [38, 39] and the regularity of solutions to the PDE plays an important role in the existence of the gradient of the cost function, see Theorem 2.

3.1 Multiphase shape optimization

Recall that $\mathcal{D}$ is a bounded, Lipschitz, simply connected, and piecewise $\mathcal{C}^1$ domain. Denote by $\mathcal{S}$ the set of singular points of $\partial \mathcal{D}$, then the outward unit normal vector ν to $\mathcal{D}$ is well-defined on $\partial \mathcal{D} \setminus \mathcal{S}$. For $r \ge 1$ we define

$$\mathcal{C}_{\partial \mathcal{D}}^r(\overline{\mathcal{D}}, \mathbb{R}^2) := \{\theta \in \mathcal{C}^r(\overline{\mathcal{D}}, \mathbb{R}^2) : \, \theta \cdot \nu = 0 \text{ on } \partial \mathcal{D} \setminus \mathcal{S} \text{ and } \theta = 0 \text{ on } \mathcal{S}\}. \tag{11}$$

Let $T \in W^{1,\infty}(\overline{\mathcal{D}} \times [0, t_0], \overline{\mathcal{D}})$ so that $T(\cdot, t) : \overline{\mathcal{D}} \to \overline{\mathcal{D}}$ is a bi-Lipschitz mapping for all $t \in [0, t_0]$ and $T(\overline{\mathcal{D}}, t) = \overline{\mathcal{D}}$ for all $t \in [0, t_0]$, hence $T(\cdot, t) : \overline{\mathcal{D}} \to \overline{\mathcal{D}}$ maps interior points onto interior points and boundary points onto boundary points; see [22, Chapter 4, Section 5.1 and Remark 5.2]. For $\Omega \in \mathbb{P}$, introduce the family of perturbed domains

$$\Omega_t := T(\Omega, t). \tag{12}$$

For a set of indices $\mathcal{K} = \{1, \ldots, \kappa\}$ and $\boldsymbol{\Omega} \in \mathbb{P}_\mathcal{K}(\mathcal{D})$, see Definition 1, we define

$$\boldsymbol{\Omega}_t := T(\boldsymbol{\Omega}, t) := \{T(\Omega_k, t)\}_{k \in \mathcal{K}}. \tag{13}$$

Note that $\boldsymbol{\Omega}_t$ is also a $\mathcal{K}$-diagram of $\mathcal{D}$ for all $t \in [0, t_0]$. Introduce $\theta := \partial_t T(\cdot, 0)$ and assume $\theta \in \mathcal{C}^1_{\partial \mathcal{D}}(\overline{\mathcal{D}}, \mathbb{R}^2)$.

Definition 2 (Shape derivative). *Let $J : \mathbb{P} \to \mathbb{R}$ be a shape functional.*

   (i) The Eulerian semiderivative of J at Ω in direction $\theta \in \mathcal{C}^1_{\partial \mathcal{D}}(\overline{\mathcal{D}}, \mathbb{R}^2)$ is defined by, when the limit exists,

$$dJ(\Omega)(\theta) := \lim_{t \searrow 0} \frac{J(\Omega_t) - J(\Omega)}{t}. \tag{14}$$

   (ii) J is said to be shape differentiable at Ω if it has a Eulerian semiderivative at Ω for all $\theta \in \mathcal{C}^1_{\partial \mathcal{D}}(\overline{\mathcal{D}}, \mathbb{R}^2)$ and the mapping

$$dJ(\Omega) : \mathcal{C}^1_{\partial \mathcal{D}}(\overline{\mathcal{D}}, \mathbb{R}^2) \to \mathbb{R}, \ \theta \mapsto dJ(\Omega)(\theta)$$

   is linear and continuous, in which case $dJ(\Omega)(\theta)$ is called the shape derivative of J at Ω in direction $\theta \in \mathcal{C}^1_{\partial \mathcal{D}}(\overline{\mathcal{D}}, \mathbb{R}^2)$.

For a multiphase functional $\mathcal{J} : \mathbb{P}_\mathcal{K}(\mathcal{D}) \to \mathbb{R}$, we define the Eulerian shape derivative $d\mathcal{J}(\boldsymbol{\Omega})(\theta)$ in a similar way as

$$d\mathcal{J}(\boldsymbol{\Omega})(\theta) := \lim_{t \searrow 0} \frac{\mathcal{J}(\boldsymbol{\Omega}_t) - \mathcal{J}(\boldsymbol{\Omega})}{t}. \tag{15}$$

Shape derivatives $dJ(\Omega)(\theta)$ can usually be written either as a boundary integral on $\partial \Omega$, called Hadamard formula or boundary expression, or as an integral on Ω called distributed shape derivative, domain expression or volumetric form of the shape derivative, see [32, 38, 39, 51]. A convenient way to work with distributed shape derivatives is to use a so-called *tensor representation* [38, 39], which we adapt here in the context of multiphase problems.

Definition 3 (Tensor representation of distributed shape derivative). *Let $\boldsymbol{\Omega} \in \mathbb{P}_\mathcal{K}(\mathcal{D})$ and assume $\mathcal{J} : \mathbb{P}_\mathcal{K}(\mathcal{D}) \mapsto \mathbb{R}$ has a shape derivative at $\boldsymbol{\Omega}$ in direction $\theta \in \mathcal{C}^1_{\partial \mathcal{D}}(\overline{\mathcal{D}}, \mathbb{R}^2)$. The shape derivative of $\mathcal{J}$ admits a first-order tensor representation if there exist a first-order tensor $S_0(\boldsymbol{\Omega}) \in L^1(\mathcal{D}, \mathbb{R}^2)$ and a second order tensor $S_1(\boldsymbol{\Omega}) \in L^1(\mathcal{D}, \mathbb{R}^{2 \times 2})$ such that for all $\theta \in \mathcal{C}^1_{\partial \mathcal{D}}(\overline{\mathcal{D}}, \mathbb{R}^2)$,*

$$d\mathcal{J}(\boldsymbol{\Omega})(\theta) = \int_\mathcal{D} S_1(\boldsymbol{\Omega}) : D\theta + S_0(\boldsymbol{\Omega}) \cdot \theta. \tag{16}$$

3.2   Derivative with respect to the Voronoi sites

In this section we compute the gradient with respect to $\mathbf{a}$ of a general function

$$\mathcal{G}(\mathbf{a}) := \mathcal{J}(\boldsymbol{\Omega}(\mathbf{a})), \tag{17}$$

where $\mathcal{J} : \mathbb{P}_\mathcal{K}(\mathcal{D}) \to \mathbb{R}$ is a multiphase shape functional and $\boldsymbol{\Omega}(\mathbf{a})$ is a Voronoi diagram, in the case where the shape derivative $d\mathcal{J}(\boldsymbol{\Omega}(\mathbf{a}))(\theta)$ admits the first-order tensor representation (16). Formally, $\mathcal{G}(\mathbf{a})$ can be seen as the composition of a function $\mathbf{a} \mapsto \boldsymbol{\Omega}(\mathbf{a})$ with a shape functional $\boldsymbol{\Omega} \mapsto \mathcal{J}(\boldsymbol{\Omega})$, hence the derivative of $\mathcal{G}(\mathbf{a})$ is obtained via a sort of chain rule. Here the derivative of $\boldsymbol{\Omega} \mapsto \mathcal{J}(\boldsymbol{\Omega})$ is obtained via the non-smooth shape calculus and the first-order tensor representation (16), while the derivative of $\mathbf{a} \mapsto \boldsymbol{\Omega}(\mathbf{a})$ follows from the theory developed in [14], developed in the more general case of minimization diagrams, which requires several non-degeneracy assumptions on the position of the sites a_i, $i \in \mathcal{K}_{\text{vor}}$. These non-degeneracy assumptions are restated below in Assumption 1. Note that the derivative of $\mathbf{a} \mapsto \boldsymbol{\Omega}(\mathbf{a})$ has to be understood as the time-derivative of a mapping T such that $T(\boldsymbol{\Omega}(\mathbf{a}), t) = \boldsymbol{\Omega}(\mathbf{a} + t\delta\mathbf{a})$, see Theorem 1.

In this section and in the rest of the paper we assume in addition that $\mathcal{D}$ is defined as the sublevel set

$$\mathcal{D} := \{x \in \mathbb{R}^2 : \ \varphi(x) < 0\}$$

5

with $\varphi(x) := \min_{\ell \in \mathcal{K}_\mathcal{D}} \varphi_\ell(x)$ and $\varphi_\ell \in \mathcal{C}^\infty(\mathbb{R}^2, \mathbb{R})$ for all $\ell \in \mathcal{K}_\mathcal{D} := \{\kappa_0 + 1, \ldots, \kappa_0 + \kappa_1\}$. For $\ell \in \mathcal{K}_\mathcal{D}$, introduce the set $\partial_\ell \mathcal{D} := \{x \in \partial \mathcal{D} : \varphi_\ell(x) = 0\}$. Then we have $\partial \mathcal{D} = \cup_{\ell \in \mathcal{K}_\mathcal{D}} \partial_\ell \mathcal{D}$. For $\{i, j, k\} \subset \mathcal{K}_{\text{vor}}$ and $\ell \in \mathcal{K}_\mathcal{D}$ let us define $Y_{ijk}(t) := \overline{\Omega_i(\mathbf{a} + t\delta\mathbf{a})} \cap \overline{\Omega_j(\mathbf{a} + t\delta\mathbf{a})} \cap \overline{\Omega_k(\mathbf{a} + t\delta\mathbf{a})}$ and $X_{ij\ell}(t) := \overline{\Omega_i(\mathbf{a} + t\delta\mathbf{a})} \cap \overline{\Omega_j(\mathbf{a} + t\delta\mathbf{a})} \cap \partial_\ell \mathcal{D}$. The set $Y_{ijk}(t)$ is a set of *interior vertices*, i.e., points in $\mathcal{D}$ at the intersection of three cells. The set $X_{ij\ell}(t)$ is a set of *boundary vertices*, i.e., points on $\partial \mathcal{D}$ at the intersection of two cells. We will write $Y_{ijk} := Y_{ijk}(0)$ and $X_{ij\ell} := X_{ij\ell}(0)$ for simplicity. The set Y_{ijk} contains at most one point, but $X_{ij\ell}$ may contain several points. For $k \in \mathcal{K}_{\text{vor}} \setminus \{i\}$ and $\ell \in \mathcal{K}_\mathcal{D}$, $E_{ik}(\mathbf{a} + t\delta\mathbf{a}) := \overline{\Omega_i(\mathbf{a} + t\delta\mathbf{a})} \cap \overline{\Omega_k(\mathbf{a} + t\delta\mathbf{a})}$ denotes an *interior edge* of the diagram $\mathbf{\Omega}(\mathbf{a} + t\delta\mathbf{a})$, while $E_{ik}(\mathbf{a} + t\delta\mathbf{a}) := \overline{\Omega_i(\mathbf{a} + t\delta\mathbf{a})} \cap \partial_\ell \mathcal{D}$ denotes a *boundary edge* of the diagram.

We now provide Assumption 1, a set of geometric assumptions that are required to avoid degenerate cases and perform the sensitivity analysis of Voronoi diagrams. These assumptions are particular cases of [14, Assumptions 4 and 5], which were provided in the more general context of minimization diagrams. In [14, Section 4], the implications of these assumptions in the case of Voronoi diagrams are discussed in details. In particular, they guarantee that the interior vertices Y_{ijk} of the Voronoi diagram belong to no more than three cells. They also eliminate the trivial situations where two cells with different indices are identical.

Assumption 1. *Suppose that:*

- *(Non-degeneracy of interfaces) There holds $\|\nabla_x \varphi_\ell(x)\| > 0$ for all $x \in \partial_\ell \mathcal{D}$ and for all $\ell \in \mathcal{K}_\mathcal{D}$, and $\|a_i - a_j\| > 0$ for all $\{i, j\} \subset \mathcal{K}_{vor}$.*

- *(Non-degeneracy of vertices) For all $\{i, j, k\} \subset \mathcal{K}_{vor}$ such that $Y_{ijk} \neq \emptyset$ we have*

$$(a_j - a_i)^\perp \cdot (a_k - a_i) \neq 0.$$

  In addition, for all $\{i, j\} \subset \mathcal{K}_{vor}$ and $\ell \in \mathcal{K}_\mathcal{D}$ and all $v \in X_{ij\ell}$ we have

$$(a_j - a_i)^\perp \cdot \nabla \varphi_\ell(v) \neq 0.$$

Under Assumption 1, the motion of the Voronoi cell $\Omega_i(\mathbf{a} + t\delta\mathbf{a})$ can be parameterized by a bi-Lipschitz mapping $T(\cdot, t)$, such that its derivative $\theta := \partial_t T(\cdot, 0)$ can be described explicitly as a function of the sites $\mathbf{a}$. This parameterization is described in the following theorem, which is a particular case of [14, Theorem 5].

Theorem 1. *Let $i \in \mathcal{K}_{vor}$ and suppose Assumption 1 holds. Then there exist $t_0 > 0$ and a mapping $T : \overline{\Omega_i(\mathbf{a})} \times [0, t_0] \to \mathbb{R}^2$ satisfying $T(\Omega_i(\mathbf{a}), t) = \Omega_i(\mathbf{a} + t\delta\mathbf{a})$, $T(E_{ik}(\mathbf{a}), t) = E_{ik}(\mathbf{a} + t\delta\mathbf{a})$ for all $k \in \mathcal{K}_{vor} \setminus \{i\}$, $T(E_{i\ell}(\mathbf{a}), t) = E_{i\ell}(\mathbf{a} + t\delta\mathbf{a})$ for all $\ell \in \mathcal{K}_\mathcal{D}$, $T(\partial\Omega_i(\mathbf{a}), t) = \partial\Omega_i(\mathbf{a} + t\delta\mathbf{a})$ and $T(\cdot, t) : \overline{\Omega_i(\mathbf{a})} \to \overline{\Omega_i(\mathbf{a} + t\delta\mathbf{a})}$ is bi-Lipschitz for all $t \in [0, t_0]$. In addition we have*

$$\theta(x) \cdot \nu(x) = \frac{\nabla_a \phi_k(x, a_k) \cdot \delta a_k - \nabla_a \phi_i(x, a_i) \cdot \delta a_i}{\|\nabla_x \phi_k(x, a_k) - \nabla_x \phi_i(x, a_i)\|} \text{ for all } x \in E_{ik}(\mathbf{a}) \text{ and all } k \in \mathcal{K}_{vor} \setminus \{i\}, \quad (18)$$

$$\theta(x) \cdot \nu(x) = 0 \text{ for all } x \in E_{i\ell}(\mathbf{a}) \text{ for all } \ell \in \mathcal{K}_\mathcal{D}, \quad (19)$$

where $\theta := \partial_t T(\cdot, 0)$, ν is the outward unit normal vector to $\Omega_i(\mathbf{a})$, and $\phi_i(x, a) := \|x - a\|^2$.

Introduce $\mathbf{\Omega}(\mathbf{a} + t\delta\mathbf{a}) := \{\Omega_k(\mathbf{a} + t\delta\mathbf{a})\}_{k \in \mathcal{K}_{\text{vor}}}$ and $\mathcal{G}(\mathbf{a} + t\delta\mathbf{a}) := \mathcal{J}(\mathbf{\Omega}(\mathbf{a} + t\delta\mathbf{a}))$. By definition of the Voronoi diagram, we have $\mathbf{\Omega}(\mathbf{a} + t\delta\mathbf{a}) \in \mathbb{P}_{\mathcal{K}_{\text{vor}}}(\mathcal{D})$ for all $t \in [0, t_0]$. In view of Theorem 1 we have $\mathbf{\Omega}(\mathbf{a} + t\delta\mathbf{a}) = T(\mathbf{\Omega}(\mathbf{a}), t) = \{T(\Omega_k(\mathbf{a}), t)\}_{k \in \mathcal{K}_{\text{vor}}}$. Recall that $\mathcal{E}_i^{\text{int}}$ denotes the set of interior edges of the cell $\Omega_i(\mathbf{a})$, i.e., edges that are included in $\mathcal{D}$. We have the following result for the gradient of $\mathcal{G}$.

Theorem 2. *Suppose Assumption 1 holds, that $\mathcal{J}$ is shape differentiable at $\mathbf{\Omega}(\mathbf{a})$ in direction $\theta := \partial_t T(\cdot, 0)$, and that the shape derivative $d\mathcal{J}(\mathbf{\Omega}(\mathbf{a}))(\theta)$ admits the first-order tensor representation (16). Assume further that $S_1(\mathbf{\Omega}(\mathbf{a})) \in W^{1,1}(\Omega_i(\mathbf{a}), \mathbb{R}^{2 \times 2})$ for all $i \in \mathcal{K}_{vor}$. Then the gradient of $\mathcal{G}(\mathbf{a})$, defined in (17), is given by*

$$\nabla \mathcal{G}(\mathbf{a}) \cdot \delta\mathbf{a} = \sum_{i \in \mathcal{K}_{vor}} \sum_{E \in \mathcal{E}_i^{\text{int}}} \int_E (S_1(\mathbf{\Omega}(\mathbf{a}))\nu \cdot \nu)|_{\partial\Omega_i(\mathbf{a})} \frac{(x - a_i) \cdot \delta a_i - (x - a_{k(i,E)}) \cdot \delta a_{k(i,E)}}{\|a_{k(i,E)} - a_i\|} dx, \quad (20)$$

where $k(i, E)$ is the index such that $E = \overline{\Omega_i(\mathbf{a})} \cap \overline{\Omega_{k(i,E)}(\mathbf{a})}$.

6

Proof. In this proof we write $\boldsymbol{\Omega}$ instead of $\boldsymbol{\Omega}(\mathbf{a})$ for simplicity. Using Theorem 1 we have $\mathcal{G}(\mathbf{a}+t\delta\mathbf{a}) = \mathcal{J}(\boldsymbol{\Omega}(\mathbf{a}+t\delta\mathbf{a})) = \mathcal{J}(T(\boldsymbol{\Omega},t))$ and in view of $\theta = \partial_t T(\cdot,0)$ we obtain

$$\nabla\mathcal{G}(\mathbf{a})\cdot\delta\mathbf{a} = \frac{d}{dt}(\mathcal{J}(\boldsymbol{\Omega}(\mathbf{a}+t\delta\mathbf{a})))|_{t=0} = d\mathcal{J}(\boldsymbol{\Omega})(\theta).$$

Since $\Omega_i(\mathbf{a})$ is Lipschitz, and using the assumption $S_1(\boldsymbol{\Omega}) \in W^{1,1}(\Omega_i(\mathbf{a}),\mathbb{R}^{2\times2})$ for all $i \in \mathcal{K}_{\mathrm{vor}}$, we can apply the divergence theorem in each $\Omega_i(\mathbf{a})$, which yields

$$d\mathcal{J}(\boldsymbol{\Omega})(\theta) = \int_{\mathcal{D}} S_1(\boldsymbol{\Omega}) : D\theta + S_0(\boldsymbol{\Omega})\cdot\theta \, dx = \int_{\mathcal{D}} \mathrm{div}(S_1(\boldsymbol{\Omega})^\mathsf{T}\theta) \, dx$$

$$= \sum_{i\in\mathcal{K}_{\mathrm{vor}}} \int_{\Omega_i(\mathbf{a})} \mathrm{div}(S_1(\boldsymbol{\Omega})^\mathsf{T}\theta) \, dx = \sum_{i\in\mathcal{K}_{\mathrm{vor}}} \int_{\partial\Omega_i(\mathbf{a})} (S_1(\boldsymbol{\Omega})\nu\cdot\nu)\theta\cdot\nu \, dx.$$

Using the fact that $\phi_i(x,a) = \|x-a\|^2$ we get $\nabla_a\phi_i(x,a_i) = -2(x-a_i)$ and, using (18),

$$\theta(x)\cdot\nu(x) = \frac{(x-a_i)\cdot\delta a_i - (x-a_{k(i,E)})\cdot\delta a_{k(i,E)}}{\|a_{k(i,E)}-a_i\|} \quad \text{for all } x \in E_{ik}(\mathbf{a}),$$

which proves the result. $\qquad\square$

Remark 1. *Note that Assumption 1 implies $\|a_{k(i,E)}-a_i\| > 0$ in (20).*

The following corollary, which is an immediate consequence of Theorem 2, is useful for the numerical implementation.

Corollary 1. *Under the assumptions of Theorem 2, we have*

$$\nabla\mathcal{G}(\mathbf{a})\cdot\delta\mathbf{a} = \sum_{i\in\mathcal{K}_{vor}}\sum_{E\in\mathcal{E}_i^{\mathrm{int}}} \delta a_{k(i,E)}\cdot g_{k,E} + \delta a_i\cdot g_{i,E}, \tag{21}$$

with

$$g_{k,E} = -\int_E (S_1(\boldsymbol{\Omega}(\mathbf{a}))\nu\cdot\nu)\frac{(x-a_{k(i,E)})}{\|a_{k(i,E)}-a_i\|}dx, \qquad g_{i,E} = \int_E (S_1(\boldsymbol{\Omega}(\mathbf{a}))\nu\cdot\nu)\frac{(x-a_i)}{\|a_{k(i,E)}-a_i\|}dx.$$

4 Derivative of cost function for the inverse potential problem

In this section, in order to simplify the notation, we take $\bar{\alpha} = 1$, $\zeta_1 = 1$ and we write u, f, h instead of u_1, f_1, h_1. The expression of the shape derivative in the case $\bar{\alpha} > 1$ and $\zeta_\alpha \neq 1$ can be obtained straightforwardly by multiplying by ζ_α and summing over $\alpha = 1, \ldots, \bar{\alpha}$. We require the following assumptions to prove shape differentiability.

Assumption 2. *Suppose:*

- $\boldsymbol{\Omega} \in \mathbb{P}_{\mathcal{K}_{vor}}(\mathcal{D})$,

- $q = q_{\boldsymbol{\Omega}} := \sum_{i\in\mathcal{K}_{vor}} q_i\chi_{\Omega_i}$,

- $f_\alpha \in H^1(\mathcal{D})$, $h_\alpha \in H^1(\mathcal{D})$ for all $\alpha = 1, \ldots, \bar{\alpha}$.

We now provide the shape derivative of the cost function $\mathfrak{J}(\boldsymbol{\Omega})$ for the inverse potential problem. We first provide the shape derivative in the general case of a $\mathcal{K}$-diagram $\boldsymbol{\Omega}$. The particular case of Voronoi diagrams is treated in the next sections.

Theorem 3 (distributed shape derivative). *Suppose Assumption 2 holds. Let $T \in W^{1,\infty}(\overline{\mathcal{D}}\times[0,t_0],\overline{\mathcal{D}})$ so that $T(\cdot,t) : \overline{\mathcal{D}} \to \overline{\mathcal{D}}$ is a bi-Lipschitz mapping for all $t \in [0,t_0]$ and $T(t,\overline{\mathcal{D}}) = \overline{\mathcal{D}}$ for all $t \in [0,t_0]$. Let $\theta := \partial_t T(\cdot,0)$ and assume $\theta \in \mathcal{C}^1_{\partial\mathcal{D}}(\overline{\mathcal{D}},\mathbb{R}^2)$. Then, the shape derivative of $\mathfrak{J}$, given by (8), at $\boldsymbol{\Omega} \in \mathbb{P}_{\mathcal{K}}(\mathcal{D})$ in direction $\theta \in \mathcal{C}^1_{\partial\mathcal{D}}(\overline{\mathcal{D}},\mathbb{R}^2)$ is*

$$d\mathfrak{J}(\boldsymbol{\Omega})(\theta) = \int_{\mathcal{D}} S_1(\boldsymbol{\Omega}) : D\theta + S_0(\boldsymbol{\Omega})\cdot\theta \, dx, \tag{22}$$

where $S_1(\mathbf{\Omega}) \in L^1(\mathcal{D}, \mathbb{R}^{2\times 2})$ and $S_0(\mathbf{\Omega}) \in L^1(\mathcal{D}, \mathbb{R}^2)$ are defined by

$$S_1(\mathbf{\Omega}) = \left[\frac{1}{2}(u - h)^2 - fp + \nabla u \cdot \nabla p + qup\right] I_d - \nabla p \otimes \nabla u - \nabla u \otimes \nabla p, \tag{23}$$

$$S_0(\mathbf{\Omega}) = (h - u)\nabla h - \nabla f. \tag{24}$$

The adjoint $p \in H_0^1(\mathcal{D})$ is solution of

$$\int_{\mathcal{D}} \nabla p \cdot \nabla w + qpw = \int_{\mathcal{D}} (h - u)w \quad \text{for all } w \in H_0^1(\mathcal{D}). \tag{25}$$

Proof. Here we will use the notation $T_t(\mathbf{x})$ instead of $T(\mathbf{x}, t)$ for simplicity. Introduce the Lagrangian $\mathcal{L} : \mathbb{P}_\mathcal{K}(\mathcal{D}) \times H_0^1(\mathcal{D}) \times H_0^1(\mathcal{D})$ as

$$\mathcal{L}(\mathbf{\Omega}, \xi, \mu) := \frac{1}{2}\int_{\mathcal{D}}(\xi - h)^2 + \int_{\mathcal{D}} \nabla \xi \cdot \nabla \mu + \int_{\mathcal{D}} q_{\mathbf{\Omega}}\xi\mu + f\mu.$$

Following the averaged adjoint method [39, 47], we introduce the shape-Lagrangian Λ using a reparameterization of $\mathcal{L}$:

$$\Lambda(t, \xi, \mu)) := \mathcal{L}(\mathbf{\Omega}_t, \xi^t, \mu^t)$$
$$= \frac{1}{2}\int_{\mathcal{D}}(\xi^t - h)^2 + \int_{\mathcal{D}} DT_t^{-\mathsf{T}} \circ T_t^{-1}(\nabla\xi) \circ T_t^{-1} \cdot DT_t^{-\mathsf{T}} \circ T_t^{-1}(\nabla\mu) \circ T_t^{-1} + \int_{\mathcal{D}} q_{\mathbf{\Omega}_t}\xi^t\mu^t - f\mu^t$$

with the notation $\xi^t := \xi \circ T_t^{-1}$ and $\mu^t := \mu \circ T_t^{-1}$.

Proceeding with the change of variables $\mathbf{x} \mapsto T_t(\mathbf{x})$ inside the integrals, we get

$$\Lambda(t, \xi, \mu) = \frac{1}{2}\int_{\mathcal{D}}(\xi - \tilde{h}(t))^2 \det(DT_t) + \int_{\mathcal{D}} \mathbb{M}(t)\nabla\xi \cdot \nabla\mu + \int_{\mathcal{D}}(q_{\mathbf{\Omega}}\xi\mu - \tilde{f}(t)\mu)\det(DT_t),$$

where $\mathbb{M}(t) := \det(DT_t)DT_t^{-1}DT_t^{-\mathsf{T}}$, $\tilde{h}(t) = h \circ T_t$, $\tilde{f}(t) = f \circ T_t$. The derivative of $\mathbb{M}(t)$ at $t = 0$ is given by, see [22, 46],

$$\mathbb{M}'(0) = \text{div}(\theta)I_d - D\theta - D\theta^{\mathsf{T}}.$$

This yields, using Assumption 2,

$$d\mathfrak{J}(\mathbf{\Omega})(\theta) = \partial_t \Lambda(0, u, p)$$
$$= \frac{1}{2}\int_{\mathcal{D}}(u - h)^2 \text{div}(\theta) + (\nabla h \cdot \theta)(h - u) + \int_{\mathcal{D}} \mathbb{M}'(0)\nabla u \cdot \nabla p + q_{\mathbf{\Omega}}up\,\text{div}(\theta)$$
$$- \int_{\mathcal{D}} fp\,\text{div}(\theta) + p\nabla f \cdot \theta.$$

Using tensor calculus, see for instance [38], we compute

$$\mathbb{M}'(0)\nabla u \cdot \nabla p = D\theta : [(\nabla u \cdot \nabla p)I_d - \nabla p \otimes \nabla u - \nabla u \otimes \nabla p]$$

The other terms of $d\mathfrak{J}(\mathbf{\Omega})(\theta)$ can be rearranged in a similar way to obtain (22). $\square$

4.1 Interface representation of the gradient

In the case of Voronoi diagrams, the state u and adjoint state p have higher regularity, which is a crucial property to compute the gradient of G.

Proposition 1. *Suppose Assumption 1 and 2 hold. Then u, p in $H^2(\mathcal{D})$, $S_1(\mathbf{\Omega}(\mathbf{a})) \in W^{1,1}(\Omega_i(\mathbf{a}), \mathbb{R}^{2\times 2})$ for all $i \in \mathcal{K}_{vor}$ and $S_0(\mathbf{\Omega}(\mathbf{a})) \in W^{1,1}(\mathcal{D}, \mathbb{R}^2)$.*

Proof. We have $-\Delta u = -qu + f$ and $-qu + f \in L^2(\mathcal{D})$ as well as $-\Delta p = -qp + (h - u)$ and $-qp + (h - u) \in L^2(\mathcal{D})$. This implies u, p in $H^2(\mathcal{D})$ since $\mathcal{D}$ is convex, applying for instance [26, Theorem 3.2.1.2]. The regularity $S_1(\mathbf{\Omega}(\mathbf{a})) \in W^{1,1}(\Omega_i(\mathbf{a}), \mathbb{R}^{2\times 2})$ and $S_0(\mathbf{\Omega}(\mathbf{a})) \in W^{1,1}(\mathcal{D}, \mathbb{R}^2)$ follows immediately from the expressions (23), (24) and the regularity of f, h, u, p. $\square$

Applying Theorem 2, Theorem 3 and Proposition 1 we obtain the following result.

Theorem 4. *Suppose Assumptions 2 and 1 hold, then the gradient of $G(\mathbf{a})$, defined in (9), is given by*

$$\nabla G(\mathbf{a}) \cdot \delta\mathbf{a} = \sum_{i \in \mathcal{K}_{vor}} \sum_{E \in \mathcal{E}_i^{\mathrm{int}}} \int_E (S_1(\mathbf{\Omega}(\mathbf{a}))\nu \cdot \nu)|_{\partial\Omega_i(\mathbf{a})} \frac{(x - a_i) \cdot \delta a_i - (x - a_{k(i,E)}) \cdot \delta a_{k(i,E)}}{\|a_{k(i,E)} - a_i\|} dx, \qquad (26)$$

where $k(i, E)$ is the index such that $E = \overline{\Omega_i(\mathbf{a})} \cap \overline{\Omega_{k(i,E)}(\mathbf{a})}$ and $S_1(\mathbf{\Omega}(\mathbf{a}))$ is given by (23).

Alternatively, $\nabla G(\mathbf{a})$ may be written in the following form, which is more amenable for numerical implementation.

Corollary 2. *Suppose Assumptions 1 and 2 hold, then*

$$\nabla G(\mathbf{a}) \cdot \delta\mathbf{a} = \sum_{i \in \mathcal{K}_{vor}} \sum_{E \in \mathcal{E}_i^{\mathrm{int}}} \delta a_{k(i,E)} \cdot g_{k,E} + \delta a_i \cdot g_{i,E}, \qquad (27)$$

with

$$g_{k,E} = -\int_E q_i up \frac{(x - a_{k(i,E)})}{\|a_{k(i,E)} - a_i\|} dx, \qquad g_{i,E} = \int_E q_i up \frac{(x - a_i)}{\|a_{k(i,E)} - a_i\|} dx.$$

Proof. Let $\mathcal{E} := \cup_{i \in \mathcal{K}_{vor}} \mathcal{E}_i^{\mathrm{int}}$ denote the set of interior edges of the Voronoi diagram (i.e., edges that are included in $\mathcal{D}$), which is the union of all interior edges of cells $\Omega_i(\mathbf{a}), i \in \mathcal{K}_{vor}$. Firstly, we can write $\nabla G(\mathbf{a})$ as in (21). Then, as each interior edge $E \in \mathcal{E}$ is at the interface of exactly two cells, whose indices we denote by $k_1(E)$ and $k_2(E)$, we can reorganize the terms in (21) by summing over all $E \in \mathcal{E}$, which yields:

$$\nabla G(\mathbf{a}) \cdot \delta\mathbf{a} = \sum_{E \in \mathcal{E}} \delta a_{k_1(E)} \cdot g_{k_1,E} + \delta a_{k_2(E)} \cdot g_{k_2,E}, \qquad (28)$$

where

$$g_{k_1,E} := \int_E [\![S_1(\mathbf{\Omega}(\mathbf{a}))\nu \cdot \nu]\!]_E \frac{(x - a_{k_1(E)})}{\|a_{k_1(E)} - a_{k_2(E)}\|} dx,$$

$$g_{k_2,E} := -\int_E [\![S_1(\mathbf{\Omega}(\mathbf{a}))\nu \cdot \nu]\!]_E \frac{(x - a_{k_2(E)})}{\|a_{k_1(E)} - a_{k_2(E)}\|} dx,$$

and $[\![S_1(\mathbf{\Omega}(\mathbf{a}))\nu \cdot \nu]\!]_E := (S_1(\mathbf{\Omega}(\mathbf{a}))\nu \cdot \nu)|_{\partial\Omega_{k_1(E)}(\mathbf{a})} - (S_1(\mathbf{\Omega}(\mathbf{a}))\nu \cdot \nu)|_{\partial\Omega_{k_2(E)}(\mathbf{a})}$.
In view of (23) we compute

$$S_1(\mathbf{\Omega}(\mathbf{a}))\nu \cdot \nu = \frac{1}{2}(u - h)^2 - fp + \nabla u \cdot \nabla p + qup - 2\partial_\nu u \partial_\nu p. \qquad (29)$$

Since u, p in $H^2(\mathcal{D})$, $f, h \in H^1(\mathcal{D})$, we can show that

$$[\![S_1(\mathbf{\Omega}(\mathbf{a}))\nu \cdot \nu]\!]_E = [\![\frac{1}{2}(u - h)^2 - fp + \nabla u \cdot \nabla p + qup - 2\partial_\nu u \partial_\nu p]\!]_E = [\![qup]\!]_E$$

$$= (qup)|_{\partial\Omega_{k_1(E)}(\mathbf{a})} - (qup)|_{\partial\Omega_{k_2(E)}(\mathbf{a})} = (q_{k_1(E)} - q_{k_2(E)})up.$$

Indeed, let us show for instance that $[\![\nabla u \cdot \nabla p]\!]_E = 0$; the other terms can be treated in a similar way. We have $\nabla u \cdot \nabla p \in W^{1,1}(\mathcal{D})$, hence $\nabla u \cdot \nabla p|_{\Omega_i(\mathbf{a})} \in W^{1,1}(\Omega_i(\mathbf{a}))$ for all $i \in \mathcal{K}_{vor}$. Since $\Omega_i(\mathbf{a})$ is Lipschitz, the trace $\mathrm{Tr} : W^{1,1}(\Omega_i(\mathbf{a})) \to L^1(\partial\Omega_i(\mathbf{a}))$ is linear and continuous, see [35], thus $\nabla u \cdot \nabla p|_{\partial\Omega_i(\mathbf{a})} \in L^1(\partial\Omega_i(\mathbf{a}))$. In addition, since $\nabla u \cdot \nabla p \in W^{1,1}(\mathcal{D})$ and using the continuity of the trace Tr, we have $\nabla u \cdot \nabla p|_{\partial\Omega_i(\mathbf{a})} = \nabla u \cdot \nabla p|_{\partial\Omega_j(\mathbf{a})}$ on the interface $E = \partial\Omega_i(\mathbf{a}) \cap \partial\Omega_j(\mathbf{a})$, for all $i, j \in \mathcal{K}_{vor}$. Therefore $[\![\nabla u \cdot \nabla p]\!]_E = 0$. Finally, rewriting the sum as in (21), we obtain (27). $\qquad\square$

4.2 Distributed expression of the gradient

In Corollary 2 we have obtained the gradient of G with the coefficients expressed as integrals on the edges E. Note however that in Theorem 3, the shape derivative is expressed as a volumetric integral. In smooth shape optimization, it is now well-known that distributed (volumetric) expressions of shape derivatives present several benefits such as higher accuracy in the context of finite elements [32] and ease of implementation [37, 39]. In the context of nonsmooth shape optimization with PDE constraints, where the solution of the PDE often has low regularity due to the presence of corners for instance, using distributed expressions of shape derivatives is particularly interesting as it demands less regularity on the data, as shown in [38]. However, in non-smooth, parameterized shape optimization, as treated here, employing the boundary expression of the shape derivative is quite natural as the restriction of θ on an edge E of the diagram is an explicit function of the parameters (here the sites $\mathbf{a}$), as in (18), which combines well with the fact that the boundary expression of the shape derivative only depends on θ and not on its derivatives [11, 13].

The dependence of the distributed expression of the shape derivative (22) on $D\theta$ complicates the writing of the gradient of G using this expression. Indeed, the expression of θ is only known explicitly on the edges E, while computing $D\theta$ necessitates describing an explicit extension of θ inside the cells. This task would pose a significant challenge in the context of a general non-smooth, parameterized shape optimization problem. However, for Voronoi diagrams, thanks to the simple geometry, a relatively straightforward procedure exists to obtain an explicit extension of θ inside the cells, which we outline here. Note that this procedure relies solely on the existence of a tensor expression (16) for the shape derivative. This property is highly general, underlining the broad applicability of the approach. The case of distributed shape derivative with boundary terms, as in [39], can also be considered via a similar procedure. To the best of our knowledge, this is the first time that a distributed expression of the shape derivative is used in the context of a non-smooth, parameterized shape optimization problem. This results in two distinct formulas (27) and (31) for ∇G. Although these formulations are mathematically equal, they lead to different discretizations and numerical implementations. In Section 5.2, we numerically compare these two formulas, thereby extending the existing literature on the comparison of shape gradients, as exemplified in [32, 51], to encompass the non-smooth case.

We start with some preliminary definitions. Since $\Omega_i(\mathbf{a})$ is convex, we can partition $\Omega_i(\mathbf{a})$ into a set of non-overlapping triangles, where the vertices of each triangle are the site a_i and two consecutive vertices of the cell, using a counterclockwise orientation. Introduce the functions $\psi_v \in C^0(\Omega_i(\mathbf{a}), \mathbb{R})$ such that $\psi_v(a_i) = 0$, $\psi_v(v) = 1$, $\psi_v(w) = 0$ for all other vertices w of the cell $\Omega_i(\mathbf{a})$, and ψ_v is linear on each of the triangle partitioning $\Omega_i(\mathbf{a})$. Due to the continuity of ψ_v, this determines ψ_v uniquely. Also, ψ_v is piecewise linear, and there are only two triangles on which ψ_v is not identically zero; we denote by $T(a_i, v, w_\ell)$ these two triangles, where w_ℓ are the two neighbouring vertices of v, for $\ell = 1, 2$.

We can compute ψ_v explicitly on each triangle $T(a_i, v, w_\ell)$. Since ψ_v is linear on $T(a_i, v, w_\ell)$, it takes the form
$$\psi_v(z) = z \cdot \beta + \gamma$$
where $z = (z_1, z_2)$ are Cartesian coordinates. We get the three equations
$$\psi_v(a_i) = a_i \cdot \beta + \gamma = 0, \qquad \psi_v(v) = v \cdot \beta + \gamma = 1, \qquad \psi_v(w) = w \cdot \beta + \gamma = 0.$$

This yields $(a_i - w) \cdot \beta = 0$, $(a_i - v) \cdot \beta = -1$ and $\beta = \lambda(a_i - w)^\perp$ with $\lambda \in \mathbb{R}$ and $(a_i - w)^\perp$ is a rotation of angle $\pi/2$ of $(a_i - w)$ in counterclockwise orientation. Then, using $(a_i - v) \cdot \beta = 1$ we get $\lambda(a_i - v) \cdot (a_i - w)^\perp = 1$ and $\lambda = 1/(a_i - v) \cdot (a_i - w)^\perp$. Using the last equation yields $\gamma = -w \cdot \beta$. Finally
$$\psi_v(z) = (z - w) \cdot \beta = -\frac{(z - w) \cdot (a_i - w)^\perp}{(a_i - v) \cdot (a_i - w)^\perp}$$

and
$$\nabla \psi_v(z) = \beta = -\frac{(a_i - w)^\perp}{(a_i - v) \cdot (a_i - w)^\perp}. \tag{30}$$

Theorem 5. *Suppose Assumptions 1 and 2 hold, then the gradient of $G(\mathbf{a})$, defined in (9), is given by*
$$\nabla G(\mathbf{a}) \cdot \delta\mathbf{a} = \sum_{i \in \mathcal{K}_{vor}} \sum_{v \in \mathcal{V}_i^{int}} \delta a_i \cdot g_i^v + \delta a_j \cdot g_j^v + \delta a_k \cdot g_k^v + \sum_{v \in \mathcal{V}_i^{bd}} \delta a_i \cdot \mathfrak{g}_i^v + \delta a_j \cdot \mathfrak{g}_j^v, \tag{31}$$

10

where $\mathcal{V}_i^{int}$ is the set of interior vertices of the cell $\Omega_i(\mathbf{a})$ and $\mathcal{V}_i^{bd}$ the set of boundary vertices, (i,j,k) are the indices of the three cells that share the common vertex v, i.e., $v = \overline{\Omega_i(\mathbf{a})} \cap \overline{\Omega_j(\mathbf{a})} \cap \overline{\Omega_k(\mathbf{a})}$, and

$$g_i^v := M_v(j,k,i)^\top I(i,v), \quad g_j^v := M_v(k,i,j)^\top I(i,v), \quad g_k^v := M_v(i,j,k)^\top I(i,v),$$

$$\mathfrak{g}_i^v := \mathcal{M}_v^\ell(j,i)^\top I(i,v), \quad \mathfrak{g}_j^v := \mathcal{M}_v^\ell(i,j)^\top I(i,v).$$

Here

$$M_v(i,j,k) := \frac{(a_i - a_j)^\perp \otimes (v - a_k)^\top}{Q(i,j,k)}, \qquad Q(i,j,k) := \det \begin{pmatrix} (a_j - a_i)^\top \\ (a_k - a_i)^\top \end{pmatrix}. \tag{32}$$

and

$$\mathcal{M}_v^\ell(j,i) := \frac{-\nabla_x \varphi_\ell(v)^\perp \otimes (v - a_i)^\top}{\det \begin{pmatrix} (a_j - a_i)^\top \\ \nabla_x \varphi_\ell(v)^\top \end{pmatrix}}. \tag{33}$$

Also,

$$
\begin{aligned}
I(i,v) := &\int_{T(a_i,v,w_1)} S_1(\mathbf{\Omega}(\mathbf{a}))\nabla\psi_v(x) + S_0(\mathbf{\Omega}(\mathbf{a}))\psi_v(x) \, dx \\
&+ \int_{T(a_i,v,w_2)} S_1(\mathbf{\Omega}(\mathbf{a}))\nabla\psi_v(x) + S_0(\mathbf{\Omega}(\mathbf{a}))\psi_v(x) \, dx
\end{aligned}
\tag{34}
$$

and w_ℓ, $\ell = 1,2$, are the two neighbouring vertices of v, relatively to cell $\Omega_i(\mathbf{a})$.

Proof. In this proof we write $\mathbf{\Omega}$ instead of $\mathbf{\Omega}(\mathbf{a})$ for simplicity. Let $\mathcal{V}_i$ be the set of vertices of the cell $\Omega_i(\mathbf{a})$, then we either have $v = Y_{ijk}(0)$ if $v \in \mathcal{V}_i$ is an interior vertex, or $v = X_{ij\ell}(0)$ if $v \in \mathcal{V}_i$ is a boundary vertex, see Section 3.2. Define $\theta_v := \frac{d}{dt}Y_{ijk}(0)$ if $v \in \mathcal{V}_i$ is an interior vertex or $\theta_v := \frac{d}{dt}X_{ij\ell}(0)$ if $v \in \mathcal{V}_i$ is a boundary vertex. Using [14, Theorem 7] we know that

$$\theta_v = M_v(j,k,i)\delta a_i + M_v(k,i,j)\delta a_j + M_v(i,j,k)\delta a_k \tag{35}$$

if $v \in \mathcal{V}_i$ is an interior vertex. Here, (i,j,k) denote the indices of the three cells of the vertex v.

If v is a boundary vertex which is not a singular point of $\partial\mathcal{D}$, then θ_v is tangential to $\partial\mathcal{D}$, and we have

$$\theta_v = \mathcal{M}_v^\ell(j,i)\delta a_i + \mathcal{M}_v^\ell(i,j)\delta a_j, \tag{36}$$

see [14, Theorem 8]. Here (i,j) are the two indices of the cells of the vertex v and φ_ℓ are the level set functions representing the edges of $\partial\mathcal{D}$, see Section 3.2. If v is a boundary vertex which is also a singular point of $\partial\mathcal{D}$, then $\theta_v = 0$.

Next, introduce

$$\theta_i(x) := \sum_{v \in \mathcal{V}_i} \theta_v \psi_v(x), \tag{37}$$

and define $\theta : \mathcal{D} \to \mathbb{R}^2$ as $\theta|_{\Omega_i(\mathbf{a})} := \theta_i$. By definition of ψ_v, one has $\theta \in W^{1,\infty}(\mathcal{D}, \mathbb{R}^2)$.

Let us introduce the mapping $T(x,t) = x + t\theta(x)$, $x \in \mathcal{D}$. Then we claim that the restriction $T|_{\Omega_i(\mathbf{a})}$ of T to the cell $\Omega_i(\mathbf{a})$ has the same properties as the mapping T of Theorem 1, in particular we have $T(\Omega_i(\mathbf{a}), t) = \Omega_i(\mathbf{a} + t\delta\mathbf{a})$, $T(\partial\Omega_i(\mathbf{a}), t) = \partial\Omega_i(\mathbf{a} + t\delta\mathbf{a})$ and $T|_{\Omega_i(\mathbf{a})}$ is bi-Lipschitz for all $t \in [0,t_0]$. We verify this claim by checking the construction of T in [14, Theorem 5], as Theorem 1 is a particular case of [14, Theorem 5]. In [14, Theorem 5], in the particular case of Voronoi diagrams, T is first defined at the vertices of the cell $\Omega_i(\mathbf{a})$ by $T(v,t) = v + t\theta_v$, where θ_v is given by (35) when v is an interior vertex, and by (36) when v is a boundary vertex. Next, $T(\cdot, t)$ is defined on each edge E of a cell $\Omega_i(\mathbf{a})$ by a linear interpolation of $T(v,t)$ and $T(w,t)$, where v,w are the extremities of E. Then, in [14, Theorem 5], $T(\cdot, t)$ is extended inside the cell $\Omega_i(\mathbf{a})$. The extension to the cell is arbitrary, as long as the bi-Lipschitz property of $T(\cdot, t)$ is preserved. In our case, the extension is explicit in view of the definition (37), and it can be check that $T(\cdot, t)$ is indeed bi-Lipschitz. Thus, the mapping $T(x,t) = x + t\theta(x)$, $x \in \mathcal{D}$, where θ is defined by (37), is valid in Theorem 1.

11

Thus, using Theorem 1 we have $G(\mathbf{a} + t\delta\mathbf{a}) = \mathfrak{J}(\mathbf{\Omega}(\mathbf{a} + t\delta\mathbf{a})) = \mathfrak{J}(T(\mathbf{\Omega}, t))$, hence

$$\nabla G(\mathbf{a}) \cdot \delta\mathbf{a} = \frac{d}{dt}(\mathfrak{J}(\mathbf{\Omega}(\mathbf{a} + t\delta\mathbf{a})))|_{t=0} = d\mathfrak{J}(\mathbf{\Omega})(\theta),$$

where $\theta = \partial_t T(\cdot, 0)$. Then by Theorem 3 and (37) we have

$$d\mathfrak{J}(\mathbf{\Omega})(\theta) = \int_{\mathcal{D}} S_1(\mathbf{\Omega}) : D\theta + S_0(\mathbf{\Omega}) \cdot \theta \, dx = \sum_{i \in \mathcal{K}_{\text{vor}}} \int_{\Omega_i(\mathbf{a})} S_1(\mathbf{\Omega}) : D\theta_i + S_0(\mathbf{\Omega}) \cdot \theta_i \, dx.$$

Next, we compute

$$D\theta_i = \sum_{v \in \mathcal{V}_i} \theta_v \otimes \nabla\psi_v$$

and

$$S_1(\mathbf{\Omega}) : D\theta_i = \sum_{v \in \mathcal{V}_i} S_1(\mathbf{\Omega}) : (\theta_v \otimes \nabla\psi_v) = \sum_{v \in \mathcal{V}_i} S_1(\mathbf{\Omega})\nabla\psi_v \cdot \theta_v.$$

This yields

$$d\mathfrak{J}(\mathbf{\Omega})(\theta) = \sum_{i \in \mathcal{K}_{\text{vor}}} \sum_{v \in \mathcal{V}_i} \theta_v \cdot \int_{\Omega_i(\mathbf{a})} S_1(\mathbf{\Omega})\nabla\psi_v(x) + S_0(\mathbf{\Omega})\psi_v(x) \, dx. \qquad (38)$$

Since $\psi_v \equiv 0$ on $\Omega_i(\mathbf{a}) \setminus \cup_{\ell=1}^2 T(a_i, v, w_\ell)$, we have, in view of (34),

$$\int_{\Omega_i(\mathbf{a})} S_1(\mathbf{\Omega})\nabla\psi_v(x) + S_0(\mathbf{\Omega})\psi_v(x) \, dx = I(i, v).$$

Thus we have obtained

$$\nabla G(\mathbf{a}) \cdot \delta\mathbf{a} = d\mathfrak{J}(\mathbf{\Omega})(\theta) = \sum_{i \in \mathcal{K}_{\text{vor}}} \sum_{v \in \mathcal{V}_i} \theta_v \cdot I(i, v) = \sum_{i \in \mathcal{K}_{\text{vor}}} \left[\sum_{v \in \mathcal{V}_i^{int}} \theta_v \cdot I(i, v) + \sum_{v \in \mathcal{V}_i^{bd}} \theta_v \cdot I(i, v). \right]$$

Finally, using (35) and (36) we obtain (31). $\qquad \square$

Remark 2. *An alternative approach to compute ∇G using the distributed expression of the shape derivative is to proceed without decomposing the integral over $\mathcal{D}$ into the Voronoi cells $\Omega_i(\mathbf{a})$ in the proof of Theorem 5. In this way, one obtains*

$$\nabla G(\mathbf{a}) \cdot \delta\mathbf{a} = d\mathfrak{J}(\mathbf{\Omega})(\theta) = \sum_{v \in \mathcal{V}} \theta_v \cdot \int_{\mathcal{D}} S_1(\mathbf{\Omega})\nabla\psi_v(x) + S_0(\mathbf{\Omega})\psi_v(x) \, dx,$$

where $\mathcal{V}$ is the set of vertices of the Voronoi diagrams. This leads to a formula similar to (31), but with a summation on $\mathcal{V}$ instead. Even though the integrals here are on $\mathcal{D}$, they are in fact calculated only on the support of ψ_v, which is small.

5 Numerical experiments

In this section we present numerical experiments to evaluate the type of optimization (inverse) problem (10) that can be solved in relation to the amount of noise in the measurements h_α, the number κ_0 of cells in the Voronoi diagram defining the ground truth $q^\star$ and the distribution (binary or not) of the values of $q^\star$ in the different cells of the diagram. We also analyze the influence of the number $\bar{\alpha}$ of available sources and the influence of the initial estimate $\mathbf{a}^0$ in the optimization process. We also evaluate whether there is any practical difference in using the distributed (31) or the interface (27) expression of the gradient when solving the optimization problem.

In all the experiments we considered $\mathcal{D} = (0, 1) \times (0, 1) \subset \mathbb{R}^2$ and generated problems with known solution such that $a_i \in \mathcal{D}$ for all $i \in \mathcal{K}_{\text{vor}} = \{1, \ldots, \kappa_0\}$. We decided to include this information

in the optimization problem and so we reformulated (10) as the finite-dimensional bound-constrained optimization problem given by

$$\underset{\mathbf{a} \in \mathbb{R}^{2\kappa_0}}{\text{Minimize}} \, G(\mathbf{a}) \text{ subject to } a_i \in \overline{\mathcal{D}} \text{ for all } i \in \mathcal{K}_{\text{vor}}. \tag{39}$$

The most natural way to solve problem (39) having ∇G available is to use the projected gradient method [10, 24, 40], described for completeness in Algorithm 1. In the algorithm, $P_{\overline{\mathcal{D}}}$ represents the projection operator on $\overline{\mathcal{D}}$. In the backtracking procedure (line 7), we choose $\lambda_{\text{new}} = \lambda/2$ for simplicity. As usual in the literature, in the numerical experiments we considered $\gamma = 10^{-4}$ for the Armijo line search constant. As a stopping criterion we considered $\|\mathbf{a}^\ell - \mathbf{a}^{\ell-1}\|_\infty \leq \epsilon$, with $\epsilon = 10^{-6}$, which corresponds to lack of progress. We would like to have used a stopping criterion asking for a small $\|\nabla G(\mathbf{a}^\ell)\|$, but as its calculation depends on the numerical resolution of two PDEs, it is difficult to obtain small values in practice. Precisely, the lack of progress is a consequence of the error in the calculations of G and ∇G.

Algorithm 1: Projected gradient method.

    Input: $\mathbf{a}^0 \in \overline{\mathcal{D}}$, $\gamma \in (0,1)$, $0 < \sigma_1 \leq \sigma_2 < 1$
    Output: $\hat{\mathbf{a}} \in \overline{\mathcal{D}}$
1 function ProjectedGradient($\mathbf{a}^0$, γ, σ_1, σ_2, $\hat{\mathbf{a}}$)
2   Set $\ell \leftarrow 0$
3   **while** *stop criteria not satisfied* **do**
4   Compute $d^\ell := P_{\overline{\mathcal{D}}}(\mathbf{a}^\ell - \nabla G(\mathbf{a}^\ell)) - \mathbf{a}^\ell$
5   Set $\lambda \leftarrow 1$
6   **while** $G(\mathbf{a}^\ell + \lambda d^\ell) \not\leq G(\mathbf{a}^\ell) + \lambda\gamma\langle\nabla G(\mathbf{a}^\ell), d^\ell\rangle$ **do**
7   Choose $\lambda_{\text{new}} \in [\sigma_1\lambda, \sigma_2\lambda]$ and set $\lambda \leftarrow \lambda_{\text{new}}$
8   Define $\mathbf{a}^{\ell+1} := \mathbf{a}^\ell + \lambda d^\ell$ and set $\ell \leftarrow \ell + 1$
9   Define $\hat{\mathbf{a}} := \mathbf{a}^\ell$

We implemented Algorithm 1 within the computing platform FEniCS [36, 43], an open-source software for solving PDEs with the finite element method. We discretize $\mathcal{D}$ using a regular grid with 128 cells in each direction and crossed diagonals. Voronoi diagrams are computed with the implementation provided in [11, 13, 14].

In the experiments, we constructed problems with known solution $q^\star$, for different values of κ_0. The construction starts by choosing κ_0 and drawing $a_i^\star \in \mathcal{D}$ for all $i \in \mathcal{K}_{\text{vor}}$. Then we set $q_i^\star$ for all $i \in \mathcal{K}_{\text{vor}}$ (as it will be shown below). Then we choose $\bar{\alpha}$, f_α for $\alpha = 1, \ldots, \bar{\alpha}$ and solve (3,4) to obtain $u_\alpha^\star$ for $\alpha = 1, \ldots, \bar{\alpha}$. The values of ζ_α for $\alpha = 1, \ldots, \bar{\alpha}$ in the definition (8) of $G(\mathbf{a})$ are computed in practice as

$$\zeta_\alpha = \frac{1}{\displaystyle\int_{\mathcal{D}} (u_\alpha(q_{\mathbf{\Omega}(\mathbf{a}^0)}) - h_\alpha)^2}.$$

In this way, the terms corresponding to each measurement h_α start with the same magnitude in the calculation of G. (As a consequence, $G(\mathbf{a}^0) = \bar{\alpha}/2$.) Synthetic measurements h_α are obtained via the formula $h_\alpha := u_\alpha^\star + \eta_\alpha$, where η_α is a normal Gaussian noise with mean zero and standard deviation $c\|u_\alpha^\star\|_\infty$ and c is a parameter that takes different values depending on the experiment. The noise level is then computed as

$$\text{Noise} = 100\% \times \left(\frac{\sum_{\alpha=1}^{\bar{\alpha}} \zeta_\alpha \|h_\alpha - u_\alpha^\star\|_{L^2(\mathcal{D})}^2}{\sum_{\alpha=1}^{\bar{\alpha}} \zeta_\alpha \|u_\alpha^\star\|_{L^2(\mathcal{D})}^2}\right)^{1/2}. \tag{40}$$

Note that the hypothesis $h_\alpha \in H^1(\mathcal{D})$ is required for the computation of the shape derivative in Theorem 3 and consequently also in Theorems 4 and 5, but is stronger than the regularity $h_\alpha \in L^2(\mathcal{D})$ expected in practice, as $h_\alpha = u_\alpha^\star + \eta_\alpha$ and the measurement noise η_α is expected to be only in $L^2(\mathcal{D})$. Nevertheless, the formulas (27) and (31) for $\nabla G(\mathbf{a})$ prove to be efficient in numerical experiments.

In order to measure the quality of a reconstruction $\hat{\mathbf{a}}$, we define a relative error metric as follows:

$$E(\hat{\mathbf{a}}) = 100\% \times \frac{\displaystyle\int_{\mathcal{D}} |q^\star - q(\hat{\mathbf{a}})|}{\displaystyle\int_{\mathcal{D}} q^\star}. \tag{41}$$

We consider that the lower the $E(\hat{\mathbf{a}})$, the better the reconstruction $\hat{\mathbf{a}}$ is.

5.1 Dependence on the number of sites

In this section, we present three types of experiments. In the first type, we reconstruct a ground truth $q^\star$ with equidistant values $q_i^\star = 10\,i$, $i = 1, \ldots \kappa_0$. In the second experiment, we reconstruct a ground truth $q^\star$ with approximately binary values $q_i^\star = 9 + i$ for $i = 1, \ldots, \lfloor \kappa_0/2 \rfloor$ and $q_i^\star = 108 - (\kappa_0 - i)$ for $i = \lfloor \kappa_0/2 \rfloor + 1, \ldots, \kappa_0$. In the third experiment, we reconstruct a ternary ground truth $q^\star$ with values $q_i^\star \in \{5, 10, 15\}$. In all cases we considered $\bar{\alpha} = 1$ and $f_1 \equiv 1$. Standard deviation parameters $c = 0$ and $c = 0.02$ were considered for the noise in (40). The initial approximation $\mathbf{a}^0$ is given by a perturbation of the known solution $\mathbf{a}^\star$ being computed as $[a_i^0]_k := P_{\overline{\mathcal{D}}}([a_i^\star]_k + r)$ for $k = 1, 2$ and all $i \in \mathcal{K}_{\mathrm{vor}}$, where $r \in (-\bar{r}, \bar{r})$ is a random number with uniform distribution and, in this experiment, $\bar{r} = 0.1$. In these experiments, we considered the boundary expressions of the shape derivative to compute ∇G.

Reconstructions for $\kappa_0 \in \{5, 6, 7, 8\}$, $\kappa_0 \in \{9, 10, 11, 12\}$, and $\kappa_0 \in \{13, 14\}$ and equidistant ground truth values are shown in Figures 1, 2, and 3, respectively. Table 1 shows some details of the optimization process. In the table, we show κ_0, the level of Noise (40) in the measurements (in %), the values of the error (41) (in %), the objective function and its gradient norm at the initial guess $\mathbf{a}^0$ and at the reconstruction $\hat{\mathbf{a}}$, the total number of iterations, the total number of evaluations of G, and the total CPU time (in seconds) used by Algorithm 1 to obtain $\hat{\mathbf{a}}$. Figures 1, 2, and 3 show that reconstructions that are visually similar to the ground truth were obtained for all cases unless $\kappa_0 = 9$, $\kappa_0 = 10$, and $\kappa_0 = 13$, which are the only cases with errors greater than 3%. In the case $\kappa_0 = 9$, the most significant difference appears in cells 1 and 2 of the solution, with $q_1^\star = 10$ and $q_2^\star = 20$, which are different from the ground truth cells. The same happens with cells 3 and 7, with $q_3^\star = 30$ and $q_7^\star = 70$, in the solution to the case $\kappa_0 = 13$. In the case $\kappa_0 = 10$, the final solution, with a large error, is different from the ground truth and can be considered the only failure of this experiment. It is worth noting that we are analyzing the solution of an optimization problem with many local non-global minimizers starting from a single initial point.

Figures 4 and 5 show reconstructions for a nearly binary ground truth with $\kappa_0 \in \{9, 10, 11, 12\}$ and $\kappa_0 \in \{13, 14\}$, respectively. Table 2 shows the details of the optimization process. In most cases, we observe a significant reduction of the error $E(\mathbf{a})$, and the reconstructions visually resemble the ground truth, the main features of the geometry are usually recovered. As κ_0 increases, we notice that there are more opportunities for combinations of cells to approximate other combinations of cells of the ground truth. For instance in Figure 4, for $\kappa_0 = 9$, one observes that the group of cells $10, 11, 12, 14$ in the reconstruction approximates the same group of cells of the ground truth, but the cells are recombined in a different way. On one hand, this provides a degree of flexibility to the reconstruction process. On the other hand, it may impair the reconstruction of small geometric features of the ground truth. By chance, in this experiment, the case $\kappa_0 = 10$ can also be considered as the only failure.

The case of a ternary ground truth, with $\kappa_0 \in \{6, 8, 10, 12\}$, is shown in Table 3 and Figure 6. Compared to the case of equidistant values, better reconstructions and smaller errors $E(\hat{\mathbf{a}})$ are obtained. We observe in addition that significant topological changes occur during the optimization. For instance in the case $\kappa_0 = 10$, the 5-valued centered cell in the initialization merges with the block of 5-valued cells on the right. As a result, the topological structure of the reconstruction's Voronoi diagram is similar or almost equal to the ground truth's Voronoi diagram in all cases. The phenomenon that a group of cells is combined in a different way to reconstruct the same group of cells in the ground truth is also observed in this case, as it was observed in the approximately binary case.

5.2 Boundary versus distributed expression of the shape derivative

In this section, we compare the boundary (27) and distributed (31) expressions of the shape derivative when applied to solve problem (39). For this purpose we considered the problems with $\kappa_0 \in \{5, 6, 7, 8\}$

κ_0	Noise	$E(\mathbf{a}^0)$	$E(\hat{\mathbf{a}})$	$G(\mathbf{a}^0)$	$G(\hat{\mathbf{a}})$	$\|\nabla G(\mathbf{a}^0)\|_2$	$\|\nabla G(\hat{\mathbf{a}})\|_2$	#iter	#feval	Time
5	0.00	13.84	0.43	0.50	0.00003	1.81954	0.00454	273	1598	1763.31
	2.19	13.84	2.01	0.50	0.03093	1.81304	0.02838	107	600	662.20
6	0.00	9.23	0.93	0.50	0.00074	0.95344	0.10760	71	515	605.92
	2.56	9.23	0.83	0.50	0.12368	0.93441	0.05933	63	425	498.60
7	0.00	14.67	0.91	0.50	0.00015	1.86209	0.00976	134	708	911.10
	2.38	14.67	1.53	0.50	0.02572	1.85186	0.01773	67	342	439.27
8	0.00	9.71	1.55	0.50	0.00077	1.61569	0.04925	142	928	1258.40
	2.71	9.71	1.92	0.50	0.09390	1.61569	0.04154	89	560	768.75
9	0.00	20.69	4.34	0.50	0.00126	2.26427	0.02300	164	836	1236.18
	2.79	20.69	7.66	0.50	0.02168	2.25165	0.04449	73	385	566.25
10	0.00	30.06	31.39	0.50	0.03640	1.74973	0.02898	66	246	390.16
	2.51	30.06	30.99	0.50	0.04050	1.74847	0.03268	133	551	865.60
11	0.00	20.61	2.19	0.50	0.00043	1.80983	0.02105	137	750	1258.29
	2.72	20.61	1.81	0.50	0.02903	1.79456	0.01728	184	1001	1687.14
12	0.00	18.49	2.47	0.50	0.00046	2.23125	0.01904	190	1040	1874.53
	2.62	18.49	2.71	0.50	0.02636	2.20879	0.01431	142	748	1368.99
13	0.00	20.55	4.54	0.50	0.00285	2.38876	0.02985	148	910	1737.56
	2.54	20.55	4.98	0.50	0.02791	2.38467	0.04890	73	423	816.54
14	0.00	10.44	2.04	0.50	0.00075	2.24406	0.02997	167	1071	2117.13
	2.74	10.44	2.23	0.50	0.03674	2.22907	0.03511	165	1055	2084.45

Table 1: Details of the reconstruction optimization process for $\kappa_0 \in \{5, 6, \ldots, 14\}$ in the case of a ground truth with equidistant values.

κ_0	Noise	$E(\mathbf{a}^0)$	$E(\hat{\mathbf{a}})$	$G(\mathbf{a}^0)$	$G(\hat{\mathbf{a}})$	$\|\nabla G(\mathbf{a}^0)\|_2$	$\|\nabla G(\hat{\mathbf{a}})\|_2$	#iter	#feval	Time
9	0.00	30.52	6.19	0.50	0.00051	2.31403	0.00783	222	881	1345.63
	3.04	30.52	6.78	0.50	0.00525	2.31193	0.01080	167	651	1017.56
10	0.00	46.92	49.10	0.50	0.05583	1.67434	0.04445	76	313	521.15
	2.83	46.92	38.62	0.50	0.01430	1.67035	0.04835	123	541	890.57
11	0.00	31.66	3.46	0.50	0.00068	2.15023	0.01538	91	514	875.21
	2.71	31.66	3.70	0.50	0.01968	2.13605	0.02308	74	415	705.93
12	0.00	22.32	6.83	0.50	0.00420	2.41077	0.04584	26	159	286.28
	2.68	22.32	6.59	0.50	0.02054	2.36726	0.03856	39	238	427.28
13	0.00	30.03	4.17	0.50	0.00143	2.59855	0.02736	65	343	643.85
	2.87	30.03	4.29	0.50	0.01778	2.59062	0.03106	31	169	317.53
14	0.00	12.57	3.40	0.50	0.00094	2.10953	0.04130	95	560	1083.03
	2.67	12.57	3.19	0.50	0.01913	2.08894	0.02402	92	540	1048.97

Table 2: Details of the reconstruction optimization process for $\kappa_0 \in \{9, 10, 11, 12, 13, 14\}$ in the case of a ground truth with approximately binary values.

κ_0	Noise	$E(\mathbf{a}^0)$	$E(\hat{\mathbf{a}})$	$G(\mathbf{a}^0)$	$G(\hat{\mathbf{a}})$	$\|\nabla G(\mathbf{a}^0)\|_2$	$\|\nabla G(\hat{\mathbf{a}})\|_2$	#iter	#feval	Time
6	2.46	9.14	0.77	0.50	0.17666	1.64958	0.00572	139	630	812.24
8	2.47	8.05	1.35	0.50	0.30222	1.22234	0.02171	175	1055	1522.91
10	2.47	20.27	8.83	0.50	0.07326	1.98013	0.01053	276	1090	1842.28
12	2.41	14.42	2.92	0.50	0.23374	2.17395	0.01457	108	608	1107.49

Table 3: Details of the reconstruction optimization process for $\kappa_0 \in \{6, 8, 10, 12\}$ in the case of a ground truth with ternary values.

Figure 1: Graphical representation of solutions found for $\kappa_0 \in \{5, 6, 7, 8\}$ in the case of a ground truth with equidistant values.
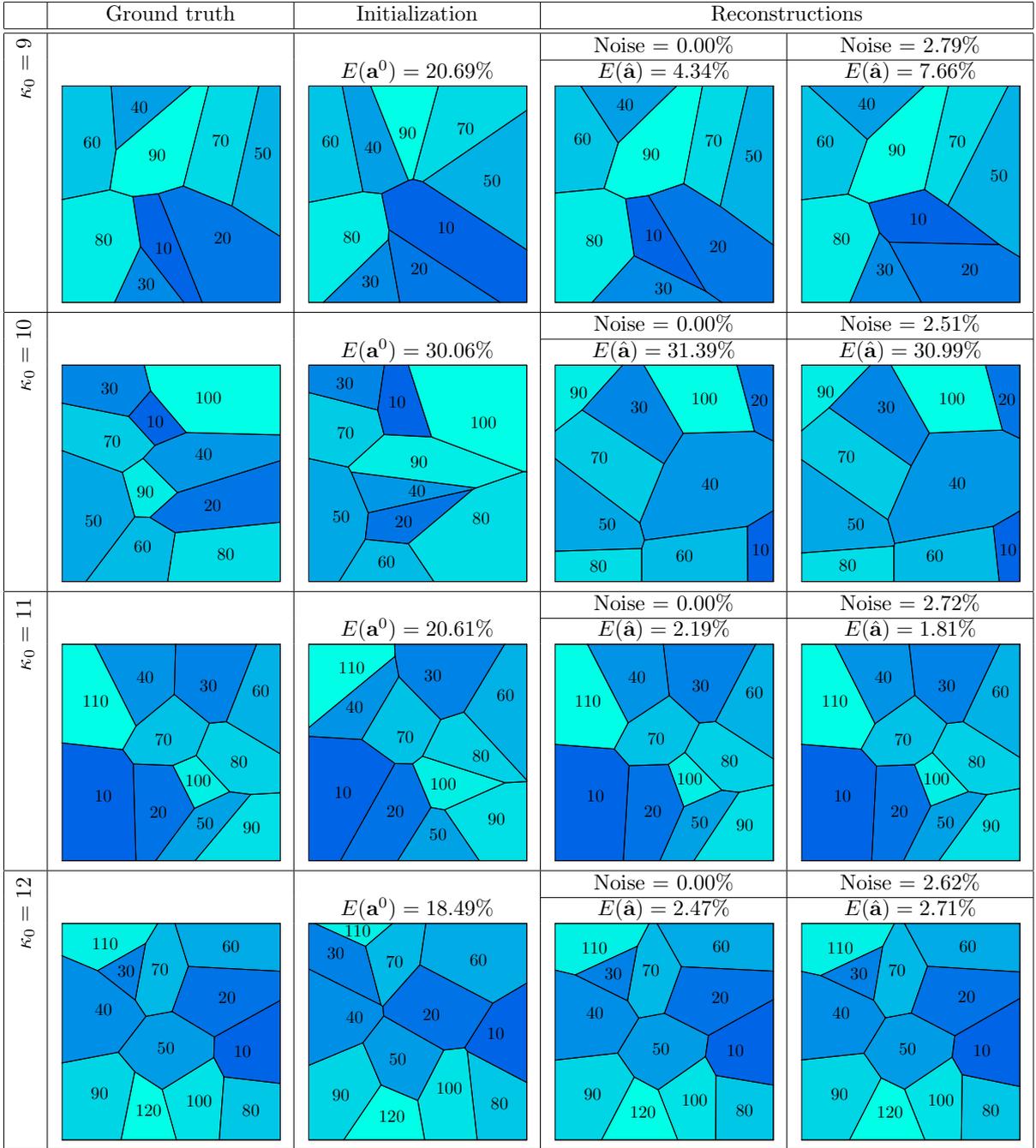
Figure 2: Graphical representation of solutions found for $\kappa_0 \in \{9, 10, 11, 12\}$ in the case of a ground truth with equidistant values.
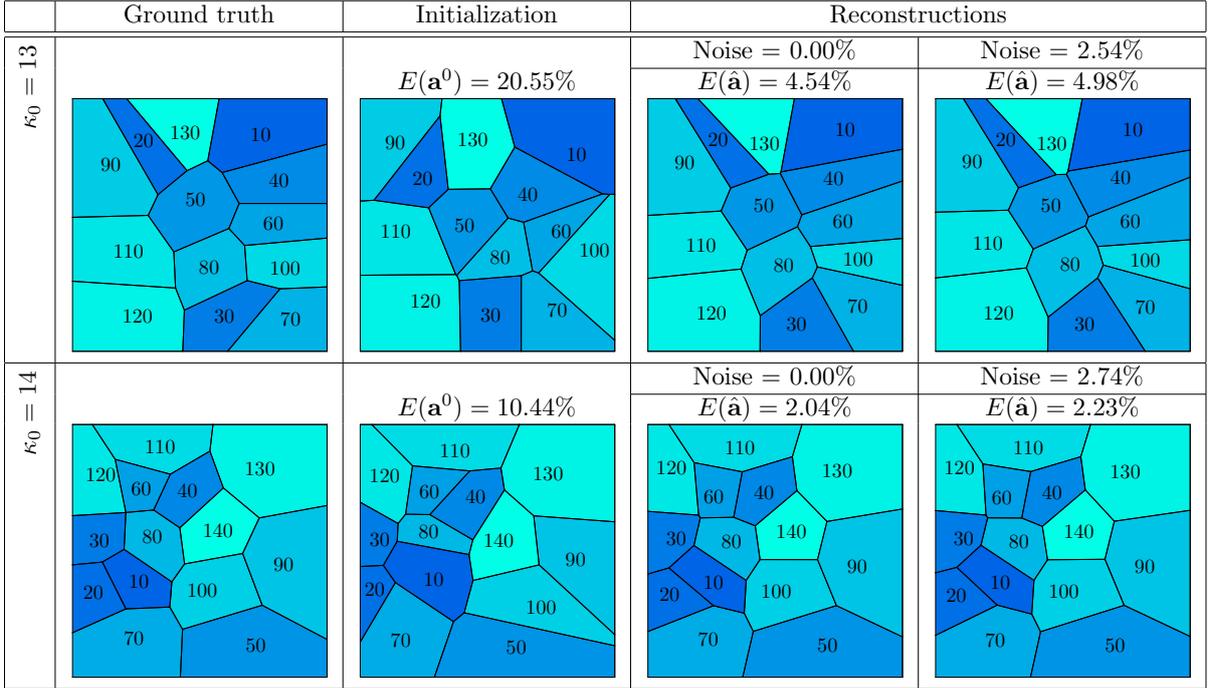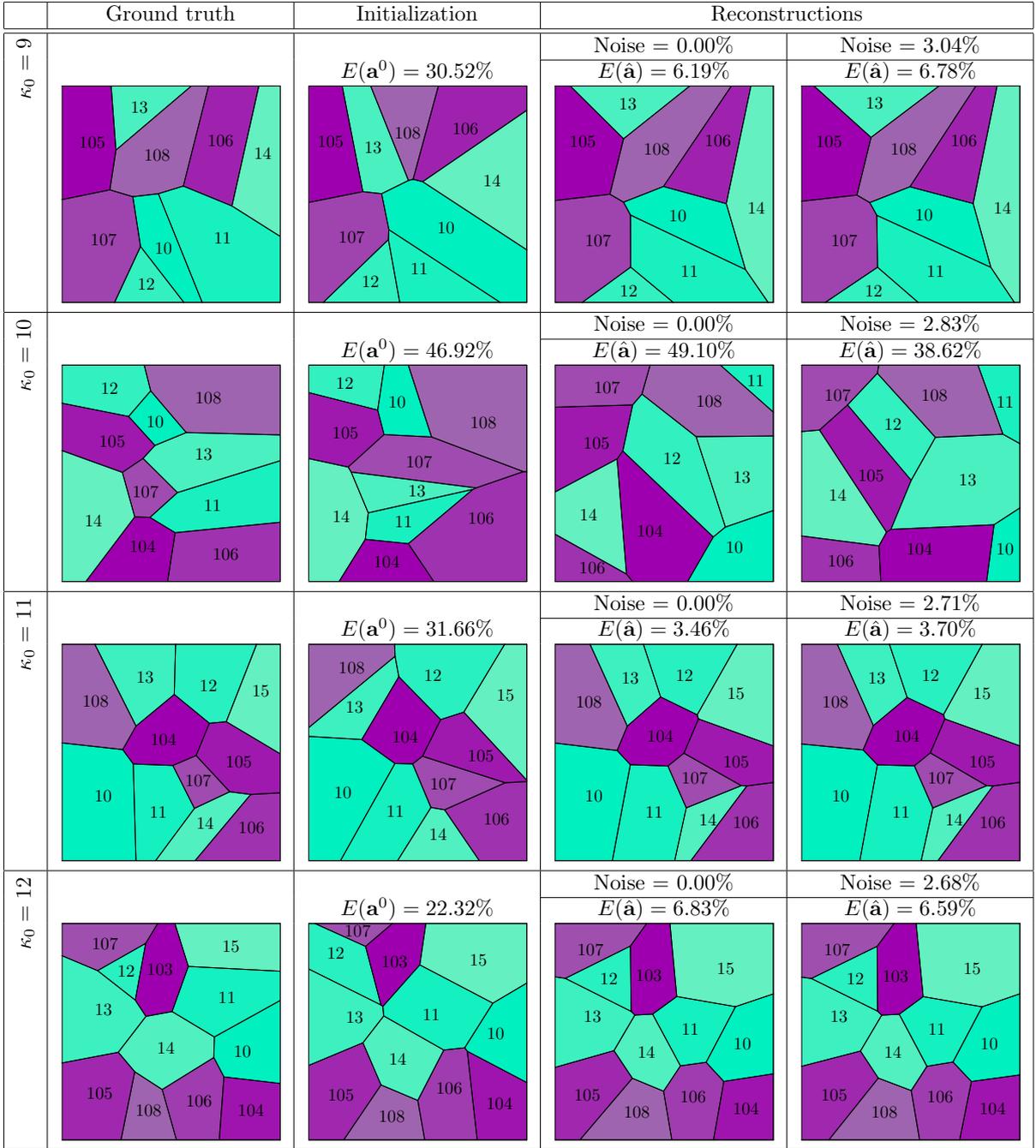
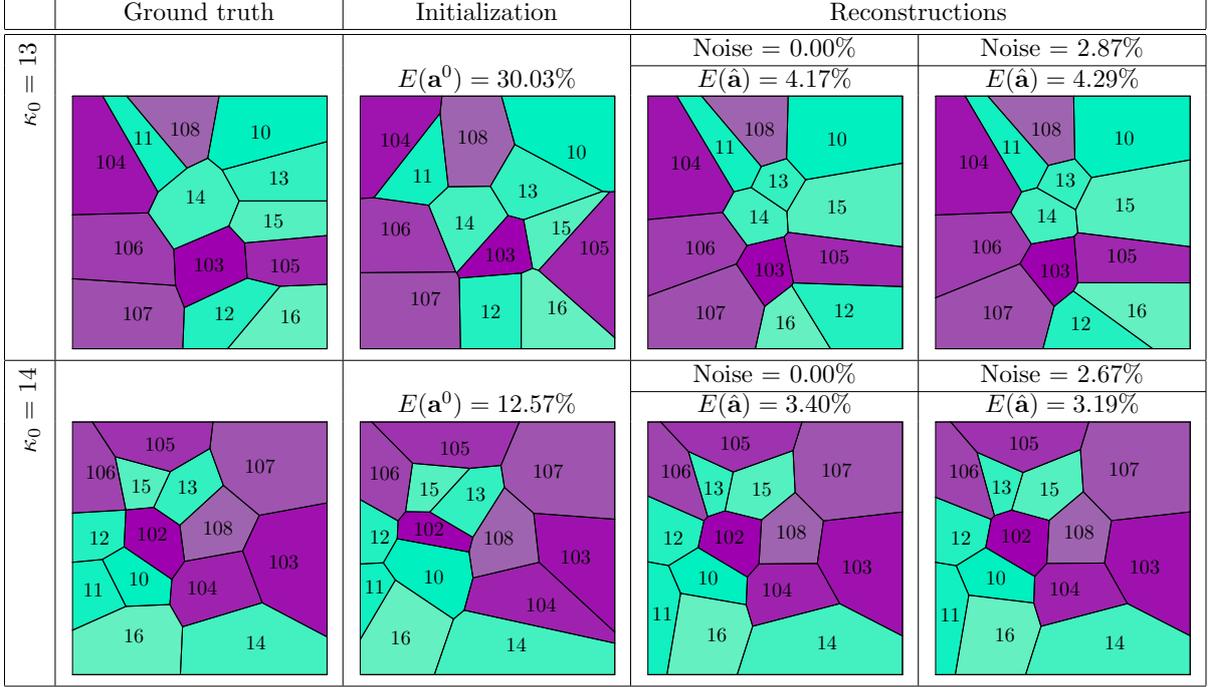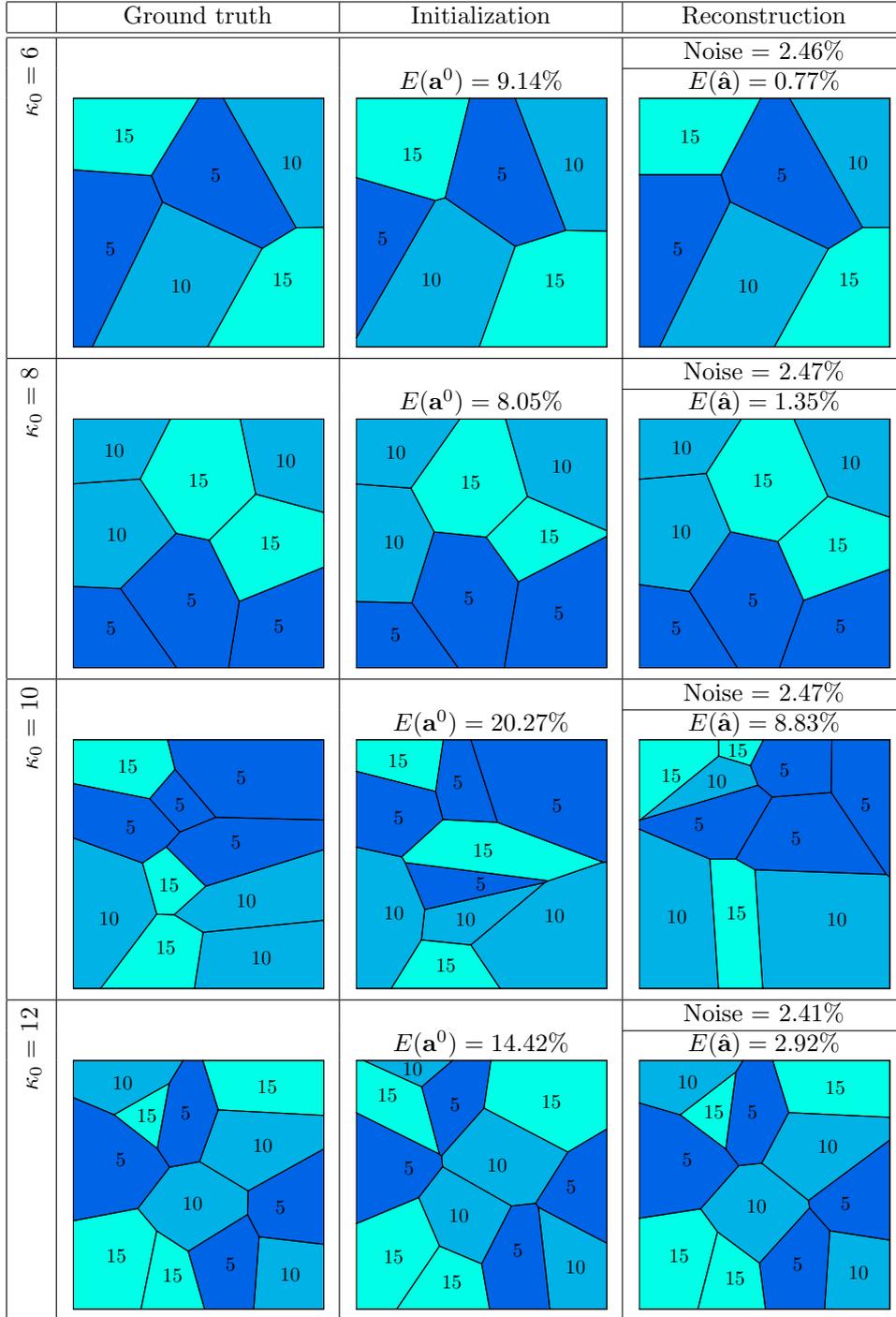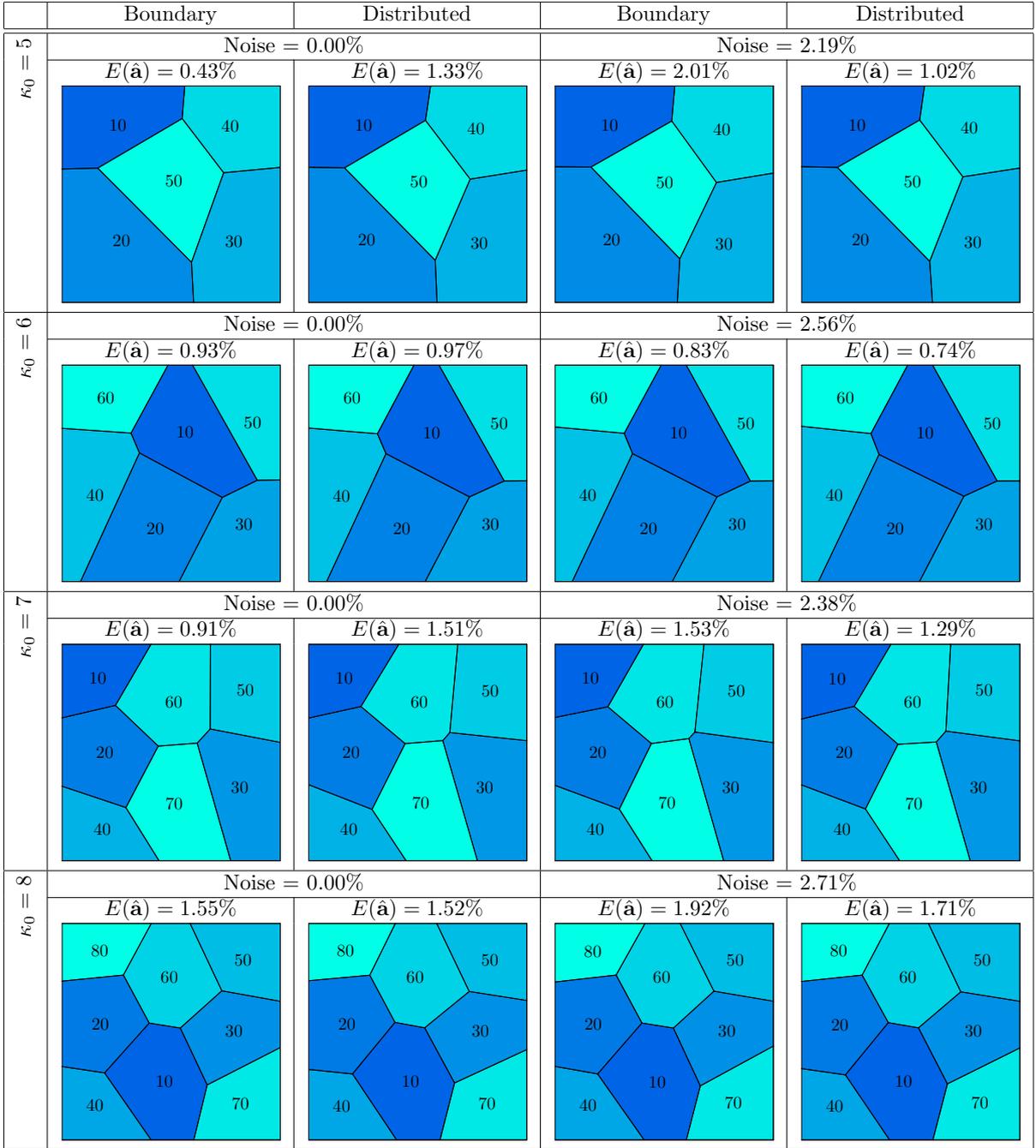Figure 3: Graphical representation of solutions found for $\kappa_0 \in \{13, 14\}$ in the case of a ground truth with equidistant values.

and a ground truth with equidistant values, whose reconstructions using the boundary expressions of the shape derivative were shown in Figure 1. These problems were solved then again using the distributed expressions of the shape derivative. Figure 7 shows the reconstructions and Table 4 shows details of the optimization process. In the figure, the reconstructions of Figure 1 are repeated for ease of comparison.

From the implementation point of view, one advantage of (31) is that one needs to compute integrals in triangles. This can be implemented in a relatively simple way using FEniCS, which provides integration in subdomains. Integration on the interfaces E in (27) is comparatively more complicated and less accurate, as the edges E do not coincide with the fixed finite element mesh. Several tools for numerical integration in lower dimensional sets are available in FEniCS and were used here to implement (27). One possible issue with (31), which is specific to the context of non-smooth, parameterized shape optimization and the procedure described in Section 4.2, is the fact that when $|v - w_1| \to 0$ or $|v - w_2| \to 0$, the triangles $T(a_i, v, w_1)$, $T(a_i, v, w_2)$ in (34) converge to a segment, while $\nabla \psi_v \to \infty$ in (34). From a numerical point of view, this may result in a large approximation error of ∇G if $|v - w_1|$ or $|v - w_2|$ gets too small.

The numerical experiments show similar reconstructions for all the cases $\kappa_0 \in \{5, 6, 7, 8\}$ considered. On one hand, the expected issue with (31) was not detrimental. On the other hand, the expected higher accuracy of (31) compared to (27) did not lead to significantly better reconstructions here. From the point of view of efficiency, for the four problems considered, the optimization process using the distributed gradient performed, on average, 93.62 iterations per problem, 5.81 function evaluations per iteration and took about 2.72 seconds for each functional evaluation. For the optimization process using the boundary expression for the gradient, these figures are 118.25, 6.08 and 0.92. This shows that by calculating the gradient in both ways, the optimization method uses approximately the same number of iterations and the same number of function evaluations per iteration. On the other hand, the calculation of the boundary gradient is three times faster than the calculation of the distributed gradient, which is why we continue to use it in all the experiments that follow.

5.3 Influence of noise on the reconstruction

In this experiment we investigate the influence of the measurements' noise on the quality of the reconstruction. For this purpose we considered problems with $\kappa_0 \in \{5, 6, 7, 8\}$ and the same characteristics as

18

Figure 4: Graphical representation of solutions found for $\kappa_0 \in \{9, 10, 11, 12\}$ in the case of a ground truth with approximately binary values.

Figure 5: Graphical representation of solutions found for $\kappa_0 \in \{13, 14\}$ in the case of a ground truth with approximately binary values.

κ_0	Noise	$E(\mathbf{a}^0)$	$E(\hat{\mathbf{a}})$	$G(\mathbf{a}^0)$	$G(\hat{\mathbf{a}})$	$\|\nabla G(\mathbf{a}^0)\|_2$	$\|\nabla G(\hat{\mathbf{a}})\|_2$	#iter	#feval	Time
5	0.00	13.84	1.33	0.50	0.00041	1.78646	0.02060	126	668	2004.47
	2.19	13.84	1.02	0.50	0.03035	1.78275	0.00965	155	819	2524.73
6	0.00	9.23	0.97	0.50	0.00079	0.91288	0.07141	55	376	1164.90
	2.56	9.23	0.74	0.50	0.12359	0.91114	0.02048	95	632	2016.80
7	0.00	14.67	1.51	0.50	0.00057	1.83739	0.01317	39	202	876.04
	2.38	14.67	1.29	0.50	0.02537	1.83023	0.00933	82	396	1746.91
8	0.00	9.71	1.52	0.50	0.00072	1.61575	0.03743	103	644	2669.31
	2.71	9.71	1.71	0.50	0.09374	1.61575	0.02631	94	577	2404.23

Table 4: Details of the reconstruction optimization process for $\kappa_0 \in \{5, 6, 7, 8\}$ in the case of a ground truth with equidistant values, using the distributed expression (31) of the shape derivative.

20

	Ground truth	Initialization	Reconstruction
$\kappa_0 = 6$		$E(\mathbf{a}^0) = 9.14\%$	Noise = 2.46% $E(\hat{\mathbf{a}}) = 0.77\%$
$\kappa_0 = 8$		$E(\mathbf{a}^0) = 8.05\%$	Noise = 2.47% $E(\hat{\mathbf{a}}) = 1.35\%$
$\kappa_0 = 10$		$E(\mathbf{a}^0) = 20.27\%$	Noise = 2.47% $E(\hat{\mathbf{a}}) = 8.83\%$
$\kappa_0 = 12$		$E(\mathbf{a}^0) = 14.42\%$	Noise = 2.41% $E(\hat{\mathbf{a}}) = 2.92\%$

Figure 6: Graphical representation of solutions found for $\kappa_0 \in \{6, 8, 10, 12\}$ in the case of a ground truth with ternary values.

Figure 7: Graphical representation of solutions found for $\kappa_0 \in \{5, 6, 7, 8\}$ in the case of a ground truth with equidistant values, using boundary and distributed expressions of the shape derivative.

the experiments of Section 5.1 using an equidistant $q^\star$. For each problem, we generated measurements with $c \in \{0.02, 0.04, 0.06, 0.08\}$ as the standard deviation parameter of the normal Gaussian noise. Figure 8 shows the reconstructions and Table 5 shows the details of the optimization process. We observe that the reconstruction seems robust with respect to noise, with an error which stays below 3%, regardless of the amount of measurement noise. The only detail that reflects the increase in noise is the final value of the objective function G. The more noise, the larger the value in the solution found. There is no observable difference in the final value of the gradient norm and in the performance of the optimization method. There are no visible changes in the number of iterations, or function evaluations or CPU time spent.

κ_0	Noise	$E(\mathbf{a}^0)$	$E(\hat{\mathbf{a}})$	$G(\mathbf{a}^0)$	$G(\hat{\mathbf{a}})$	$\|\nabla G(\mathbf{a}^0)\|_2$	$\|\nabla G(\hat{\mathbf{a}})\|_2$	#iter	#feval	Time
5	2.19	13.84	2.01	0.5	0.03093	1.81304	0.02838	107	600	743.75
	4.38	13.84	1.50	0.5	0.10236	1.79497	0.01934	200	1089	1221.48
	6.56	13.84	2.15	0.5	0.18319	1.77692	0.02092	108	552	612.08
	8.75	13.84	2.28	0.5	0.25305	1.65214	0.01776	45	226	253.42
6	2.56	9.23	0.83	0.5	0.12368	0.93441	0.05933	63	425	504.25
	5.13	9.23	1.21	0.5	0.28469	0.91478	0.03519	65	399	479.47
	7.69	9.23	1.27	0.5	0.37462	0.90778	0.01974	74	416	498.05
	10.26	9.23	1.59	0.5	0.42110	0.90519	0.00545	111	556	667.13
7	2.38	14.67	1.53	0.5	0.02572	1.85186	0.01773	67	342	449.23
	4.76	14.67	1.06	0.5	0.08749	1.83275	0.00716	144	704	916.24
	7.14	14.67	1.86	0.5	0.16196	1.77916	0.01821	46	224	296.63
	9.52	14.67	1.72	0.5	0.22969	1.64012	0.01108	78	363	474.73
8	2.71	9.71	1.92	0.5	0.09390	1.61569	0.04154	89	560	762.38
	5.42	9.71	2.65	0.5	0.23972	1.53948	0.04857	100	572	791.70
	8.12	9.71	1.88	0.5	0.33614	1.31973	0.01556	110	574	791.26
	10.83	9.71	1.95	0.5	0.39209	1.15650	0.01232	113	545	758.87

Table 5: Details of the reconstruction optimization process for $\kappa_0 \in \{5, 6, 7, 8\}$ in the case of a ground truth $q^\star$ with equidistant values, considering different levels of noise in the measurements.

5.4 Influence of initialization

In this section we analyze the influence of the initial approximations $\mathbf{a}^0$ of the solution on the optimization process. Varying the way of calculating the initial approximation, we will consider the problems with ground truth with equidistant values and $\kappa_0 \in \{9, 10\}$, with approximately binary values and $\kappa_0 \in \{9, 10, 12\}$ and with ternary values and $\kappa_0 = 10$. Those are all the problems for which, in Section 5.1, we found solutions with errors greater than 5%. All problems' details are as described in Section 5.1.

In a first experiment, we consider 100 points that are perturbations of the ground truth, evaluate G (considering $\zeta_1 = 1$) at each one and choose as the starting point of a single optimization process the point with the smallest value of G. Figures 9, 10, and 11 and Table 6 show the details. In the case of equidistant ground truth, with $\kappa_0 = 9$ the error went from 7.66% to 28.90% while, with $\kappa_0 = 10$, it went from 30.99% to 2.81% (for both cases compare Figures 2 and 9 or Tables 1 and 6). That is, one was better and the other worse suggesting that the choice of the initial point as a function of the value of G corresponds to a random choice among the alternatives considered. In the case of the approximately binary ground truth, the instance with $\kappa_0 = 9$ was worse, the instance with $\kappa_0 = 10$ improved and the instance with $\kappa_0 = 12$ remained almost the same (for the three cases, compare Figures 4 and 10 or Tables 2 and 6), while in the case of a ternary ground truth with $\kappa_0 = 10$, it improved (compare Figures 6 and 11 or Tables 3 and 6). The point is that, as the figures show, choosing the initial configuration taking into account the value of G does not correspond to choosing an initial point whose Voronoi diagram has a similar structure to the Voronoi diagram of the ground truth. Since the optimization method has difficulties in making structural changes, this makes the reconstruction difficult. In any case, in 4 out of the 6 problems considered, solutions with acceptable errors were found.

In a second experiment, we considered ten points that are perturbations of the ground truth. But instead of choosing just one as the starting point of the optimization process, we optimized ten times,
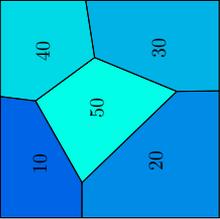
Figure 8: Graphical representation of solutions found for $\kappa_0 \in \{5, 6, 7, 8\}$ in the case of a ground truth $q^\star$ with equidistant values, considering different levels of noise in the measurements.
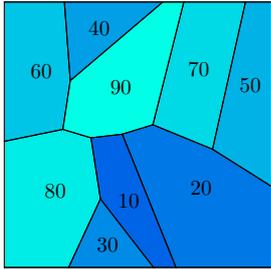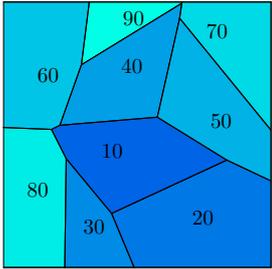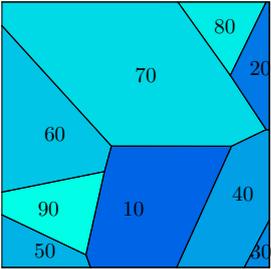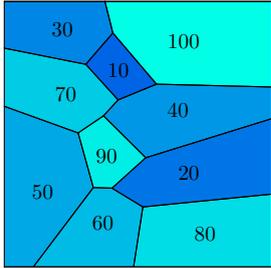
Figure 9: Graphical representation of solutions found for $\kappa_0 \in \{9, 10\}$ in the case of a ground truth with equidistant values. One-hundred perturbations of the ground truth were considered and the one with smallest value of G was used as a starting point for a single optimization process.

starting from each of them. Table 7 shows the details of the ten optimization processes and Figures 12, 13, and 14 show, among the ten, the one with the smallest error. The table and the figures show that in all cases at least one solution with a small error was found. Moreover, for all instances at least half of the 10 initial configurations led to solutions with error less than 5% and solutions with errors greater than 10% are rare. It is worth noting that this experiment is the first to find solutions with error less than 5% for all instances of Section 5.1 for which this had not yet been achieved. It should be noted that in most cases the structure of the Voronoi diagram of the initial point is very similar but not identical to that of the ground truth. The table shows two additional columns on the right side with the values of G (considering $\zeta_1 = 1$) evaluated at each initial and final point of the optimization process. The information at the final point shows that there is a good correlation between the lowest values of G and the lowest errors and that the few solutions with large errors also have a value of G that is about one order of magnitude larger than the others. This means that, in the real situation where the ground truth is not known, choosing the solution with the smallest value of G is a reasonable choice. The exception to this rule is the case with ternary ground truth. In this case, regardless of the error, all solutions have very close G values. The value of G (considering $\zeta_1 = 1$) at the starting point of the optimization process serves to show that, in this experiment, if we had chosen as the only starting point the point with the lowest value of G, we would have found solutions with reasonable errors. This contrasts the result of the previous experiment, showing that the choice of the initial point based on the value of G is quite random.

5.5 Several sources

In this section we analyze the influence of considering an increasing number of sources $\bar{\alpha} \in \{1, 2, 3, 4\}$ with $f_1(x, y) = 1$, $f_2(x, y) = \cos(\pi x) \cos(\pi y)$, $f_3(x, y) = \sin(\pi x) \sin(\pi y)$ and $f_4(x, y) = \cos(2\pi x) \cos(2\pi y)$. We consider the problems with ground truth with equidistant values and $\kappa_0 \in \{9, 10\}$, with approximately binary values and $\kappa_0 \in \{9, 10, 12\}$ and with ternary values and $\kappa_0 = 10$. Those are all the same problems considered in the previous section for which, in Section 5.1, we found solutions with errors greater than
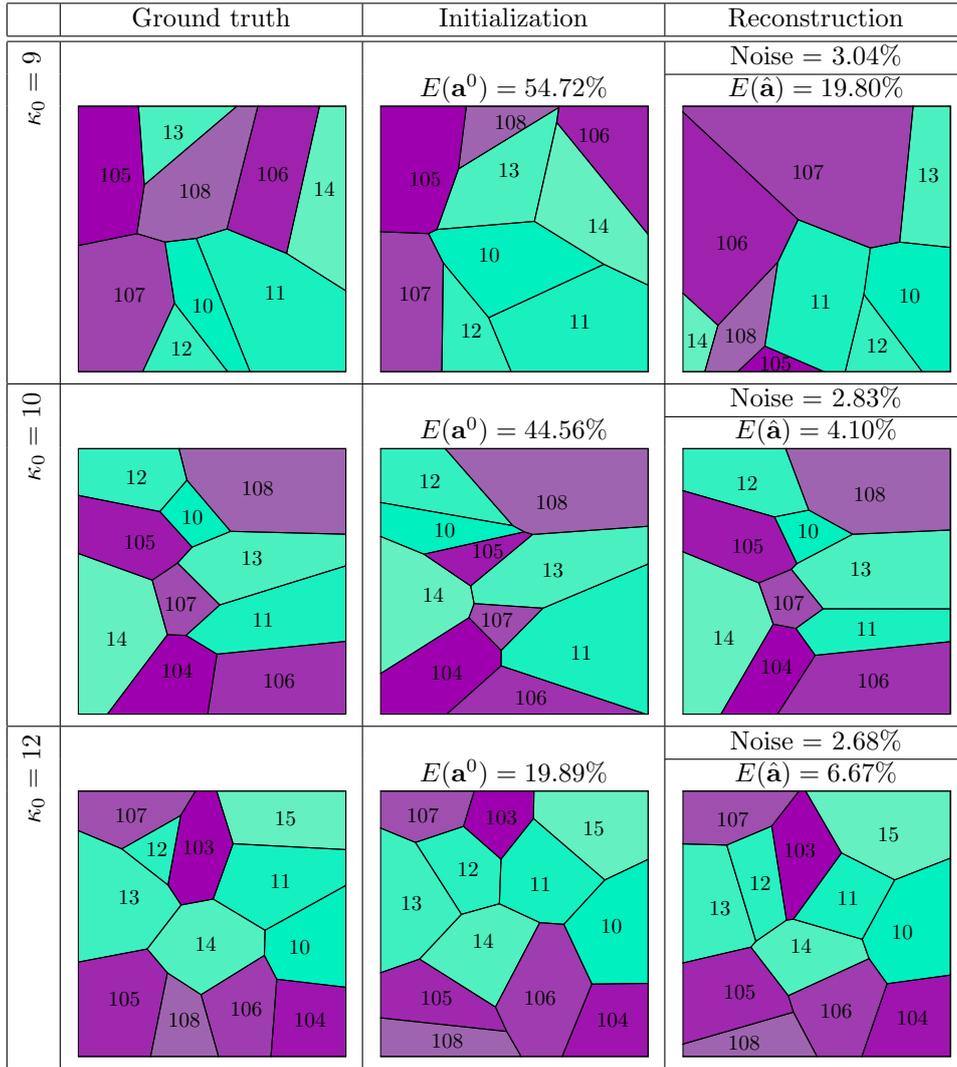
Figure 10: Graphical representation of solutions found for $\kappa_0 \in \{9, 10, 12\}$ in the case of a ground truth with approximately binary values. One-hundred perturbations of the ground truth were considered and the one with smallest value of G was used as a starting point for a single optimization process.
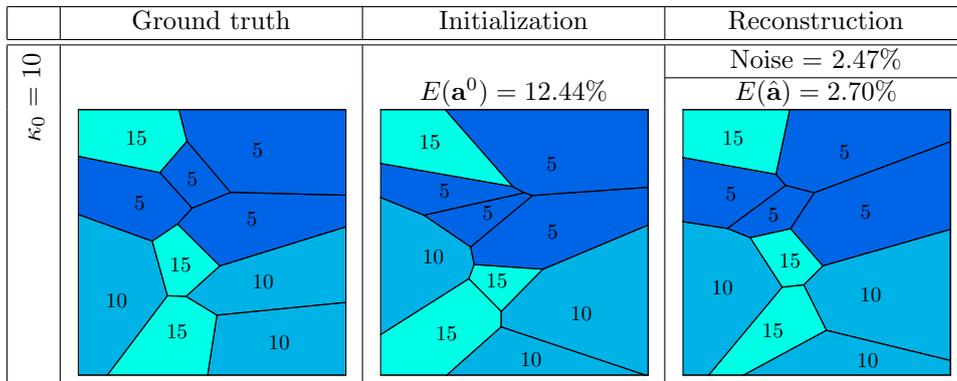

Figure 11: Graphical representation of solutions found for $\kappa_0 = 10$ in the case of a ground truth with approximately ternary values. One-hundred perturbations of the ground truth were considered and the one with smallest value of G was used as a starting point for a single optimization process.
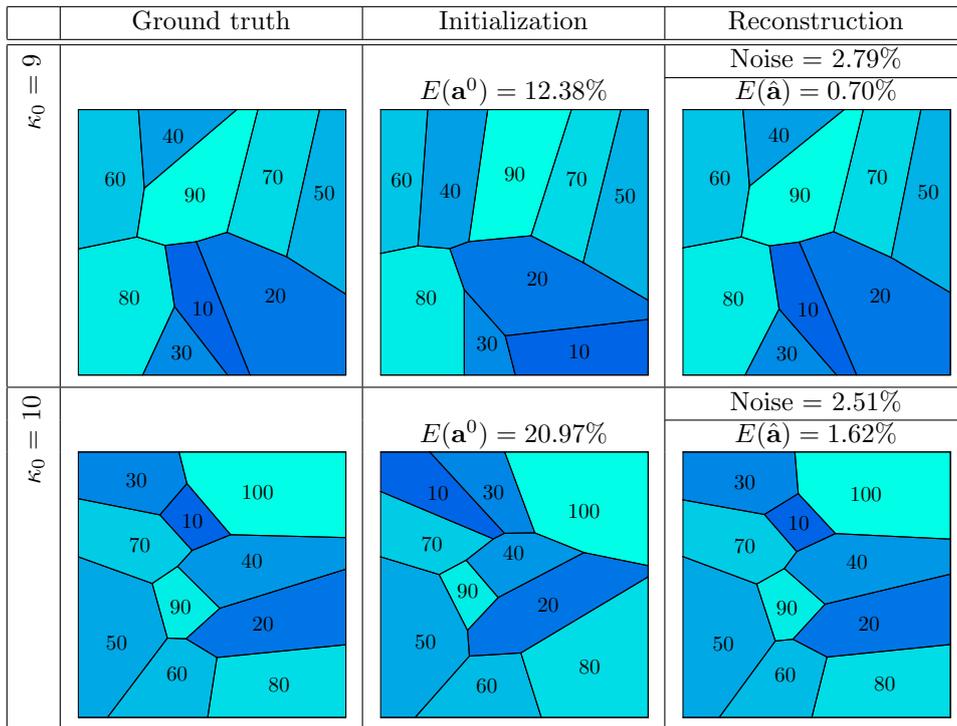
Figure 12: Graphical representation of solutions found for $\kappa_0 \in \{9, 10\}$ in the case of a ground truth with equidistant values. As a starting point, ten different ground truth perturbations were considered. The ten initial points were used to run the optimization process and the solution with the lowest error among the ten solutions is reported in this figure.
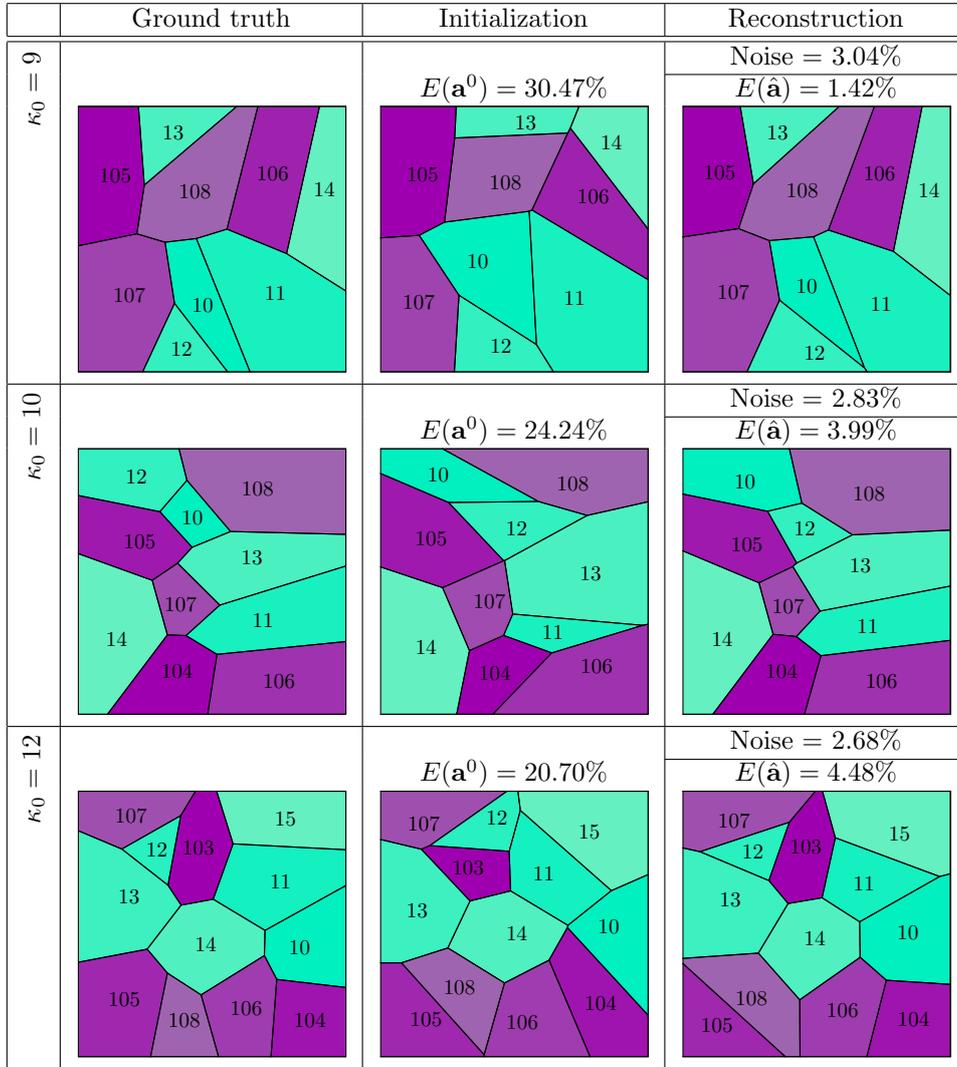
Figure 13: Graphical representation of solutions found for $\kappa_0 \in \{9, 10, 12\}$ in the case of a ground truth with approximately binary values. As a starting point, ten different ground truth perturbations were considered. The ten initial points were used to run the optimization process and the solution with the lowest error among the ten solutions is reported in this figure.

$q^\star$-type	κ_0	Noise	$E(\mathbf{a}^0)$	$E(\hat{\mathbf{a}})$	$G(\mathbf{a}^0)$	$G(\hat{\mathbf{a}})$	$\|\nabla G(\mathbf{a}^0)\|_2$	$\|\nabla G(\hat{\mathbf{a}})\|_2$	#iter	#feval	Time
equidistant	9	2.79	28.87	28.90	0.50	0.01355	2.35283	0.02953	68	256	545.80
	10	2.51	24.97	2.81	0.50	0.01732	2.05052	0.02153	137	853	1524.46
approximately binary	9	3.04	54.72	19.80	0.50	0.00295	2.12215	0.00390	97	310	629.72
	10	2.83	44.56	4.10	0.50	0.00901	1.98682	0.01970	175	1110	1978.35
	12	2.68	19.89	6.67	0.50	0.00938	2.23653	0.03176	118	665	1390.28
ternary	10	2.47	12.44	2.70	0.50	0.35750	1.99988	0.02127	80	469	922.58

Table 6: Details of the reconstruction optimization process for problems with a ground truth with equidistant values and $\kappa_0 \in \{9, 10\}$, with approximately binary values and $\kappa_0 \in \{9, 10, 12\}$ and with ternary values and $\kappa_0 = 10$. One-hundred perturbations of the ground truth were considered and the one with smallest value of G was used as a starting point for a single optimization process.
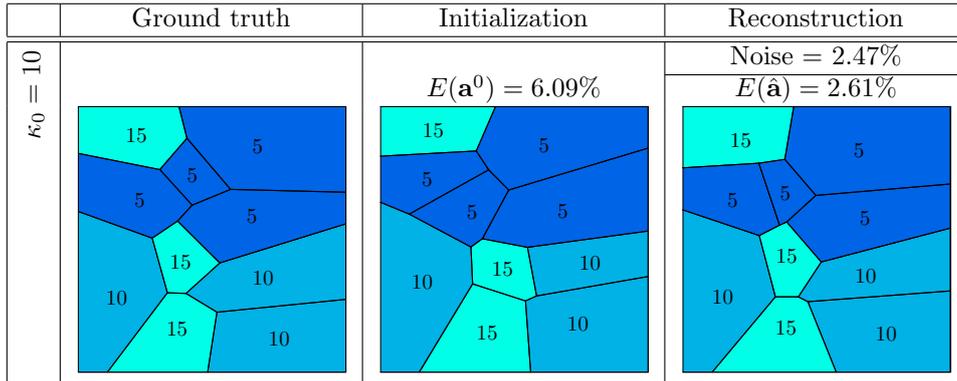

Figure 14: Graphical representation of solutions found for $\kappa_0 = 10$ in the case of a ground truth with ternary values. As a starting point, ten different ground truth perturbations were considered. The ten initial points were used to run the optimization process and the solution with the lowest error among the ten solutions is reported in this figure.

5%. In these experiments we resume the use of a single ground truth perturbation as the starting point, exactly as we did in Section 5.1. Table 8 and Figures 15 and 16 show the results. The results show that in almost all cases the increase in the number of sources helps to reduce the reconstruction error. Specifically, in 4 out of the 6 instances, errors smaller than 5% were found, in another case the error was reduced from 38.62% to 7.30% and in the other, whose error with a single source was 7.66%, a solution with error 5.52% was found. That is, acceptable solutions were found for all problematic instances of Section 5.1 by increasing the number of sources and using a single starting point. This indicates that the optimization process is able to perform major topological changes in the diagram if enough data is provided. For small $\bar{\alpha}$, the cost functional is much more "flat", and topological changes are less likely to occur.

6 Concluding remarks

In this work we have presented a general technique to compute the gradient of a cost function with respect to the sites of a Voronoi diagram, involving a PDE constraint. We have considered the specific PDE (1),(2), but we emphasize that the general procedure described here applies to a variety of PDEs, following the procedure of Section 3, as long as the shape derivative admits a first-order tensor representation (16). It can also be extended to more general scenarios, such as the case where the tensor representation of the shape derivative contains boundary terms. An important part of the study is related to the conditions required to prove the differentiability of the cost function. There are essentially two types of conditions. On one hand one needs geometric assumptions on the Voronoi diagrams as in [14], to avoid degenerate case. These conditions are independent of the considered PDE. On the other hand, the non-smoothness of the shape may also results in the low regularity of the solution to the PDE, which needs to be investigated using the theory of regularity of PDEs in nonsmooth domains, see for instance [26].
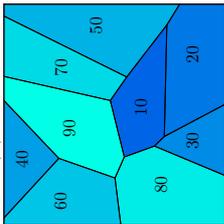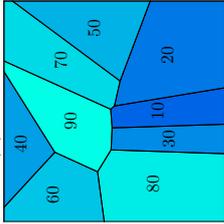
Figure 15: Graphical representation of solutions found for different number of sources $\bar{\alpha} \in \{1, 2, 3, 4\}$, and for $\kappa_0 \in \{9, 10\}$ in the case of a ground truth with equidistant values, and for $\kappa_0 = 10$ with ternary values. As initial guess of the optimization process, a single random perturbation of the known solution was considered.

Figure 16: Graphical representation of solutions found for $\kappa_0 \in \{9, 10, 12\}$ and different number of sources $\bar{\alpha} \in \{1, 2, 3, 4\}$ in the case of a ground truth with approximately binary values. As initial guess of the optimization process, a single random perturbation of the known solution was considered.

31

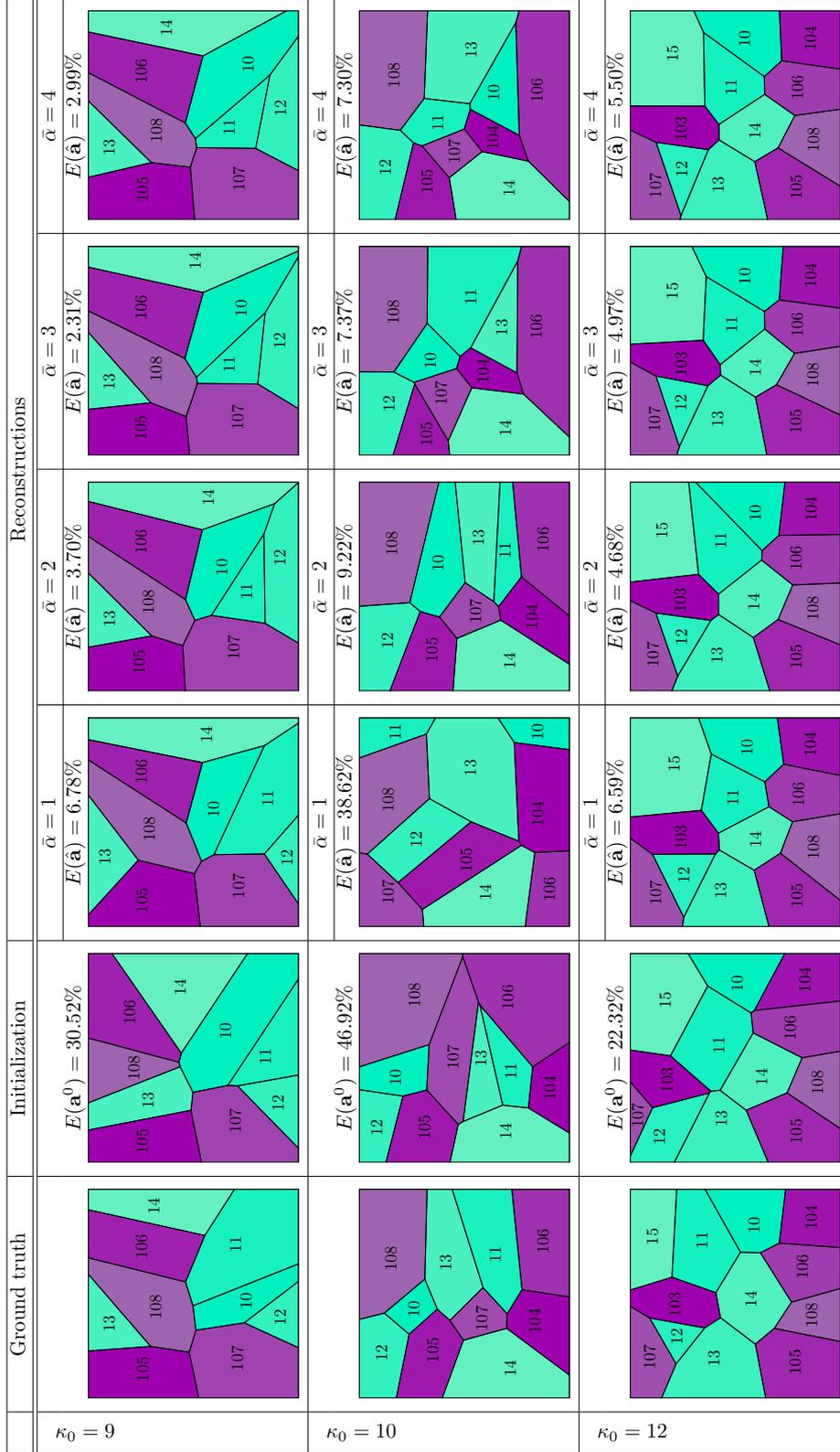| $q^\star$-type	κ_0	Noise	$E(\mathbf{a}^0)$	$E(\hat{\mathbf{a}})$	$G(\mathbf{a}^0)$	$G(\hat{\mathbf{a}})$	$\|\nabla G(\mathbf{a}^0)\|_2$	$\|\nabla G(\hat{\mathbf{a}})\|_2$	#iter	#feval	Time	$G_{\zeta_1=1}(\mathbf{a}^0)$	$G_{\zeta_1=1}(\hat{\mathbf{a}})$
equidistant	9	2.79	20.69	7.66	0.50	0.02168	2.25165	0.04449	73	385	594.66	2.247e-06	9.744e-08
			14.11	1.22	0.50	0.04524	2.17540	0.02380	198	1449	2164.65	7.018e-07	6.350e-08
			18.53	2.77	0.50	0.03035	2.16966	0.01722	139	896	1352.06	1.059e-06	6.428e-08
			17.75	2.58	0.50	0.07972	1.96174	0.05386	152	1114	1640.26	4.020e-07	6.410e-08
			12.38	0.70	0.50	0.06251	2.36750	0.01724	253	1960	2871.50	5.060e-07	6.326e-08
			12.37	2.62	0.50	0.06537	2.39397	0.06061	98	688	1005.50	4.929e-07	6.445e-08
			13.85	2.73	0.50	0.04199	2.31933	0.01809	241	1598	2302.33	7.622e-07	6.401e-08
			17.78	22.74	0.50	0.01523	2.09750	0.02241	210	845	1263.22	5.251e-06	1.599e-07
			17.84	7.04	0.50	0.00931	2.26242	0.01205	347	1334	2022.85	4.072e-06	7.584e-08
			13.98	2.11	0.50	0.12367	1.83097	0.10668	141	1134	1650.42	2.597e-07	6.424e-08
	10	2.51	30.06	30.99	0.50	0.04050	1.74847	0.03268	133	551	875.12	3.969e-06	3.215e-07
			17.52	6.63	0.50	0.04649	1.99953	0.08009	96	672	1023.79	6.035e-07	5.612e-08
			18.28	12.02	0.50	0.06740	2.06981	0.15213	65	421	649.67	7.342e-07	9.897e-08
			33.52	35.69	0.50	0.03316	1.63470	0.01601	247	950	1525.50	4.022e-06	2.667e-07
			19.27	2.47	0.50	0.01673	1.99936	0.02725	159	907	1426.29	1.374e-06	4.596e-08
			27.11	4.53	0.50	0.01058	1.70627	0.02408	52	231	368.18	2.454e-06	5.194e-08
			20.97	1.62	0.50	0.02275	2.14858	0.02457	92	561	867.60	9.955e-07	4.530e-08
			20.79	4.18	0.50	0.02060	1.78776	0.03910	88	503	779.48	1.170e-06	4.820e-08
			14.50	3.39	0.50	0.04103	2.16126	0.20650	45	302	463.04	5.845e-07	4.797e-08
			11.65	3.38	0.50	0.07718	2.20282	0.19012	385	3590	5466.33	3.179e-07	4.907e-08
approximately binary	9	3.04	30.52	6.78	0.50	0.00525	2.31193	0.01080	167	651	1028.78	7.961e-06	8.359e-08
			20.85	5.08	0.50	0.01407	2.31795	0.04048	61	355	552.87	2.928e-06	8.241e-08
			28.63	3.50	0.50	0.01736	2.25607	0.01753	213	1351	2150.59	2.253e-06	7.822e-08
			25.66	7.49	0.50	0.02262	2.06925	0.09054	75	563	855.18	2.011e-06	9.099e-08
			18.49	2.21	0.50	0.01484	2.48066	0.03832	91	641	992.81	2.559e-06	7.593e-08
			20.10	2.29	0.50	0.02963	2.39882	0.03723	79	557	849.32	1.287e-06	7.627e-08
			18.08	5.06	0.50	0.04064	2.29829	0.10399	73	506	778.28	9.972e-07	8.105e-08
			27.57	14.03	0.50	0.00625	2.50771	0.00745	98	383	602.39	1.028e-05	1.285e-07
			30.47	1.42	0.50	0.00778	2.21906	0.01127	59	309	476.44	4.839e-06	7.526e-08
			30.27	3.46	0.50	0.02452	1.31121	0.02487	113	742	1093.87	1.578e-06	7.738e-08
	10	2.83	46.92	38.62	0.50	0.01430	1.67035	0.04835	123	541	869.54	1.324e-05	3.785e-07
			24.24	3.99	0.50	0.02147	2.10296	0.05204	100	706	1103.12	1.759e-06	7.552e-08
			25.48	4.53	0.50	0.04665	2.42858	0.11593	131	1015	1591.40	8.275e-07	7.721e-08
			48.97	22.50	0.50	0.00766	1.56896	0.05317	115	641	1026.31	1.465e-05	2.244e-07
			29.85	4.21	0.50	0.00675	1.72378	0.01787	206	1042	1686.94	5.446e-06	7.357e-08
			41.93	34.23	0.50	0.02509	1.74048	0.11557	89	441	706.18	1.084e-05	5.439e-07
			27.04	8.10	0.50	0.01277	2.07238	0.02697	145	874	1389.48	3.260e-06	8.325e-08
			30.67	4.50	0.50	0.01316	1.82515	0.02631	123	752	1194.71	2.801e-06	7.370e-08
			20.61	4.19	0.50	0.02690	2.27662	0.08991	123	883	1393.14	1.383e-06	7.442e-08
			20.98	4.08	0.50	0.03998	2.36341	0.15123	136	1058	1659.59	9.602e-07	7.678e-08
	12	2.68	22.32	6.59	0.50	0.02054	2.36726	0.03856	39	238	417.90	2.555e-06	1.050e-07
			18.81	7.24	0.50	0.02341	2.18230	0.10002	128	973	1697.41	2.474e-06	1.159e-07
			22.72	4.70	0.50	0.01014	2.66081	0.00990	172	910	1612.45	4.497e-06	9.122e-08
			15.07	5.50	0.50	0.02854	2.32395	0.07616	99	667	1171.49	1.635e-06	9.332e-08
			23.58	4.85	0.50	0.01614	2.31006	0.11270	89	598	1041.11	2.965e-06	9.571e-08
			23.24	6.48	0.50	0.02605	1.66134	0.04762	127	835	1429.81	1.782e-06	9.283e-08
			22.44	6.92	0.50	0.01098	2.17625	0.01611	101	510	893.57	4.235e-06	9.297e-08
			20.70	4.48	0.50	0.01955	1.93144	0.03594	72	418	717.09	2.316e-06	9.059e-08
			24.50	6.01	0.50	0.02233	2.38237	0.10374	33	213	370.18	2.266e-06	1.012e-07
			25.07	5.12	0.50	0.01059	2.42781	0.01522	87	426	744.71	4.238e-06	8.978e-08
ternary	10	2.47	20.27	8.83	0.50	0.07326	1.98013	0.01053	276	1090	1765.31	1.808e-06	2.649e-07
			23.58	3.36	0.50	0.12253	2.18414	0.00671	99	414	675.85	1.060e-06	2.598e-07
			15.30	3.81	0.50	0.25652	1.76845	0.01097	66	359	573.34	5.066e-07	2.599e-07
			43.52	15.01	0.50	0.02879	1.87430	0.01723	140	755	1197.14	4.903e-06	2.823e-07
			7.64	5.31	0.50	0.45975	1.60664	0.42615	95	916	1420.59	2.888e-07	2.655e-07
			26.32	10.51	0.50	0.06937	1.85737	0.02567	69	355	565.96	1.915e-06	2.657e-07
			17.47	4.16	0.50	0.21353	2.00257	0.00642	132	593	965.55	6.083e-07	2.598e-07
			6.09	2.61	0.50	0.38199	1.55587	0.03179	64	398	630.69	3.398e-07	2.596e-07
			12.78	3.36	0.50	0.26112	1.78592	0.01921	78	454	714.41	4.974e-07	2.598e-07
			10.75	6.48	0.50	0.42308	1.39645	0.14314	226	2013	3114.90	3.119e-07	2.639e-07

Table 7: Details of the reconstruction optimization process for problems with a ground truth with equidistant values and $\kappa_0 \in \{9, 10\}$, approximately binary values and $\kappa_0 \in \{9, 10, 12\}$, and ternary values and $\kappa_0 = 10$. As a starting point, ten different ground truth perturbations were considered. Details for each run are shown in the table.

The optimization method considered in the present work generates a sequence of approximations $\mathbf{a}^0, \mathbf{a}^1, \ldots$ with monotonically decreasing values $G(\mathbf{a}^0), G(\mathbf{a}^1), \ldots$. This allows the method to make only a limited number of structural changes in the underlying Voronoi diagram, that impairs the reconstruction when the structure of the initial approximation is very different from the structure of the solution. One possibility would be to consider a method that generates a non-monotone sequence, such as the Spectral

$q^\star$-type	κ_0	Noise	$\bar\alpha$	$E(\mathbf{a}^0)$	$E(\hat{\mathbf{a}})$	$G(\mathbf{a}^0)$	$G(\hat{\mathbf{a}})$	$\|\nabla G(\mathbf{a}^0)\|_2$	$\|\nabla G(\hat{\mathbf{a}})\|_2$	#iter	#feval	Time
equidistant	9	2.79	1	20.69	7.66	0.50	0.02168	2.25165	0.04449	73	385	594.62
		2.79	2	20.69	7.91	1.00	0.10157	2.46801	0.35205	53	343	582.44
		2.87	3	20.69	5.52	1.50	0.11999	2.55183	0.21924	54	402	744.15
		2.88	4	20.69	9.66	2.00	0.18163	2.54418	1.10158	34	216	440.13
	10	2.51	1	30.06	30.99	0.50	0.04050	1.74847	0.03268	133	551	912.64
		2.51	2	30.06	10.40	1.00	0.03758	2.11336	0.06287	188	1337	2370.04
		2.58	3	30.06	3.36	1.50	0.03992	2.24366	0.05044	191	1434	2735.07
		2.58	4	30.06	2.63	2.00	0.06799	2.33959	0.05628	175	1170	2499.17
binary	9	3.04	1	30.52	6.78	0.50	0.00525	2.31193	0.01080	167	651	1015.95
		3.04	2	30.52	3.70	1.00	0.04779	2.40173	0.05853	75	439	756.74
		3.11	3	30.52	2.31	1.50	0.05246	2.37294	0.02904	117	730	1354.31
		3.12	4	30.52	2.99	2.00	0.06569	2.43374	0.07138	123	794	1602.16
	10	2.83	1	46.92	38.62	0.50	0.01430	1.67035	0.04835	123	541	888.71
		2.83	2	46.92	9.22	1.00	0.02008	2.37240	0.06856	178	1290	2248.01
		2.91	3	46.92	7.37	1.50	0.02237	2.41675	0.17131	61	387	766.46
		2.91	4	46.92	7.30	2.00	0.03246	2.45351	0.07032	90	606	1315.48
	12	2.68	1	22.32	6.59	0.50	0.02054	2.36726	0.03856	39	238	430.57
		2.68	2	22.32	4.68	1.00	0.07542	2.75518	0.12123	71	480	948.40
		2.76	3	22.32	4.97	1.50	0.10256	2.98346	0.24436	72	521	1103.33
		2.76	4	22.32	5.50	2.00	0.14879	2.98346	0.22073	45	341	781.84
ternary	10	2.47	1	20.27	8.83	0.50	0.07326	1.98013	0.01053	276	1090	1801.61
		2.47	2	20.27	3.22	1.00	0.44693	2.19639	0.00620	190	847	1587.51
		2.53	3	20.27	3.61	1.50	0.52475	2.25095	0.01518	132	632	1319.58
		2.53	4	20.27	4.20	2.00	0.65070	2.24876	0.02063	95	495	1116.13

Table 8: Details of the reconstruction optimization process for problems with a ground truth with equidistant values and $\kappa_0 \in \{9, 10\}$, approximately binary values and $\kappa_0 \in \{9, 10, 12\}$, and ternary values and $\kappa_0 = 10$. As initial guess of the optimization process, a single random perturbation of the known solution was considered.

Projected Gradient (SPG) [15, 16]. SPG uses a specific initial step, named Raydan-Barzilai-Borwein step [6, 44, 45], for the first attempt in the direction of the projected gradient. This specific step carries some kind of second-order information. Therefore, to increase the chances of this step being accepted, SPG uses a non-monotone Armijo criterion [25]. We will study the possibility of using SPG as the optimization method in a future work.

References

[1] Y. F. Albuquerque, A. Laurain, and K. Sturm. A shape optimization approach for electrical impedance tomography with point measurements. *Inverse Problems*, 36(9):095006, 27, 2020.

[2] H. Ammari, J. Garnier, V. Jugnon, and H. Kang. Stability and resolution analysis for a topological derivative based imaging functional. *SIAM Journal on Control and Optimization*, 50(1):48–76, 2012.

[3] H. Ammari and H. Kang. *Reconstruction of small inhomogeneities from boundary measurements*, volume 1846 of *Lecture Notes in Mathematics*. Springer-Verlag, Berlin, 2004.

[4] P. F. Ash and E. D. Bolker. Recognizing dirichlet tessellations. *Geometriae Dedicata*, 19(2):175–206, 1985.

[5] M. Bachmayr and M. Burger. Iterative total variation schemes for nonlinear inverse problems. *Inverse Problems*, 25(10):105004, 26, 2009.

[6] J. Barzilai and J. M. Borwein. Two-point step size gradient methods. *IMA Journal of Numerical Analysis*, 8(1):141–148, 1988.

[7] E. Beretta and C. Cavaterra. Identifying a space dependent coefficient in a reaction-diffusion equation. *Inverse Problems and Imaging*, 5(2):285–296, 2011.

[8] E. Beretta, M. V. de Hoop, E. Francini, and S. Vessella. Stable determination of polyhedral interfaces from boundary data for the Helmholtz equation. *Communications in Partial Differential Equations*, 40(7):1365–1392, 2015.

[9] E. Beretta, S. Micheletti, S. Perotto, and M. Santacesaria. Reconstruction of a piecewise constant conductivity on a polygonal partition via shape optimization in EIT. *Journal of Computational Physics*, 353:264–280, 2018.

[10] D. P. Bertsekas. On the goldstein-levitin-polyak gradient projection method. *IEEE Transactions on Automatic Control*, 21(2):174–184, 1976.

[11] E. G. Birgin, A. Laurain, R. Massambone, and A. G. Santana. A shape optimization approach to the problem of covering a two-dimensional region with minimum-radius identical balls. *SIAM Journal on Scientific Computing*, 43(3):A2047–A2078, January 2021.

[12] E. G. Birgin, A. Laurain, R. Massambone, and A. G. Santana. A shape optimization approach to the problem of covering a two-dimensional region with minimum-radius identical balls. *SIAM Journal on Scientific Computing*, 43(3):A2047–A2078, 2021.

[13] E. G. Birgin, A. Laurain, R. Massambone, and A. G. Santana. A shape-Newton approach to the problem of covering with identical balls. *SIAM Journal on Scientific Computing*, 44(2):A798–A824, 2022.

[14] E. G. Birgin, A. Laurain, and T. C. Menezes. Sensitivity analysis and tailored design of minimization diagrams. *Mathematics of Computation*, 92(344):2715–2768, 2023.

[15] E. G. Birgin, J. M. Martínez, and M. Raydan. Nonmonotone spectral projected gradient methods on convex sets. *SIAM Journal on Optimization*, 10(4):1196–1211, 2000.

[16] E. G. Birgin, J. M. Martínez, and M. Raydan. Algorithm 813: Spg—software for convex-constrained optimization. *ACM Transactions on Mathematical Software*, 27(3):340–349, 2001.

[17] D. P. Bourne, A. J. Mulholland, S. Sahu, and K. M. M. Tant. An inverse problem for Voronoi diagrams: a simplified model of non-destructive testing with ultrasonic arrays. *Mathematical Methods in the Applied Sciences*, 44(5):3727–3745, 2021.

[18] A. Canelas, A. Laurain, and A. A. Novotny. A new reconstruction method for the inverse potential problem. *Journal of Computational Physics*, 268:417–431, 2014.

[19] A. Canelas, A. Laurain, and A. A. Novotny. A new reconstruction method for the inverse source problem from partial boundary measurements. *Inverse Problems*, 31(7):075009, 24, 2015.

[20] D.-H. Chen, D. Jiang, and J. Zou. Convergence rates of Tikhonov regularizations for elliptic and parabolic inverse radiativity problems. *Inverse Problems*, 36(7):075001, 21, 2020.

[21] M. Choulli. Some stability inequalities for hybrid inverse problems. *Comptes Rendus Mathématique. Académie des Sciences. Paris*, 359:1251–1265, 2021.

[22] M. C. Delfour and J.-P. Zolésio. *Shapes and geometries*, volume 22 of *Advances in Design and Control*. Society for Industrial and Applied Mathematics (SIAM), Philadelphia, PA, second edition, 2011. Metrics, analysis, differential calculus, and optimization.

[23] H. W. Engl, K. Kunisch, and A. Neubauer. Convergence rates for Tikhonov regularisation of nonlinear ill-posed problems. *Inverse Problems*, 5(4):523–540, 1989.

[24] A. A. Goldstein. Convex programming in hilbert space. *Bulletin of the American Mathematical Society*, 70(5):709–710, 1964.

[25] L. Grippo, F. Lampariello, and S. Lucidi. A nonmonotone line search technique for Newton's method. *SIAM Journal on Numerical Analysis*, 23(4):707–716, 1986.

[26] P. Grisvard. *Elliptic problems in nonsmooth domains*, volume 24 of *Monographs and Studies in Mathematics*. Pitman (Advanced Publishing Program), Boston, MA, 1985.

[27] D. N. Hào and T. N. T. Quyen. Convergence rates for Tikhonov regularization of coefficient iden-
tification problems in Laplace-type equations. *Inverse Problems*, 26(12):125014, 23, 2010.

[28] B. Harrach and M. Ullrich. Monotonicity-based shape reconstruction in electrical impedance to-
mography. *SIAM Journal on Mathematical Analysis*, 45(6):3382–3403, 2013.

[29] A. Hauptmann, M. Santacesaria, and S. Siltanen. Direct inversion from partial-boundary data in
electrical impedance tomography. *Inverse Problems*, 33(2):025009, 26, 2017.

[30] F. Hettlich and W. Rundell. Iterative methods for the reconstruction of an inverse potential problem.
Inverse Problems, 12(3):251–266, 1996.

[31] M. Hintermüller and A. Laurain. Electrical impedance tomography: from topology to shape. *Control
and Cybernetics*, 37(4):913–933, 2008.

[32] R. Hiptmair, A. Paganini, and S. Sargheini. Comparison of approximate shape gradients. *BIT*,
55(2):459–485, 2015.

[33] B. Jin, X. Lu, Q. Quan, and Z. Zhou. Convergence rate analysis of Galerkin approximation of
inverse potential problem. *Inverse Problems*, 39(1):015008, 26, 2023.

[34] B. Jin and Z. Zhou. An inverse potential problem for subdiffusion: stability and reconstruction.
Inverse Problems, 37(1):015006, 26, 2021.

[35] P. Domenico Lamberti and L. Provenzano. On trace theorems for Sobolev spaces. *Matematiche
(Catania)*, 75(1):137–165, 2020.

[36] H. P. Langtangen and A. Logg. *Solving PDEs in Python: The FEniCS Tutorial I*. Simula Springer-
Briefs on Computing. Springer International Publishing, 2017.

[37] A. Laurain. A level set-based structural optimization code using FEniCS. *Structural and Multidis-
ciplinary Optimization*, 58(3):1311–1334, 2018.

[38] A. Laurain. Distributed and boundary expressions of first and second order shape derivatives in
nonsmooth domains. *Journal de Mathématiques Pures et Appliquées*, 134:328–368, 2020.

[39] A. Laurain and K. Sturm. Distributed shape derivative *via* averaged adjoint method and applica-
tions. *ESAIM. Mathematical Modelling and Numerical Analysis*, 50(4):1241–1267, 2016.

[40] E. S. Levitin and B. T. Polyak. Constrained minimization methods. *USSR Computational Mathe-
matics and Mathematical Physics*, 6(5):1–50, 1966.

[41] D. Liu and J. Du. Shape and topology optimization in electrical impedance tomography via moving
morphable components method. *Structural and Multidisciplinary Optimization*, 64(2):585–598, 2021.

[42] D. Liu, A. K. Khambampati, S. Kim, and K. Y. Kim. Multi-phase flow monitoring with electrical
impedance tomography using level set based method. *Nuclear Engineering and Design*, 289:108–116,
2015.

[43] A. Logg, K.-A. Mardal, and G. N. Wells, editors. *Automated Solution of Differential Equations by
the Finite Element Method*, volume 84 of *Lecture Notes in Computational Science and Engineering*.
Springer, 2012.

[44] M. Raydan. On the barzilai and borwein choice of steplength for the gradient method. *IMA Journal
of Numerical Analysis*, 13(3):321–326, 1993.

[45] M. Raydan. The barzilai and borwein gradient method for the large scale unconstrained minimiza-
tion problem. *SIAM Journal on Optimization*, 7(1):26–33, 1997.

[46] J. Sokołowski and J.-P. Zolésio. *Introduction to shape optimization*, volume 16 of *Springer Series in
Computational Mathematics*. Springer-Verlag, Berlin, 1992. Shape sensitivity analysis.

[47] K. Sturm. Minimax Lagrangian approach to the differentiability of nonlinear PDE constrained shape functions without saddle point assumption. *SIAM Journal on Control and Optimization*, 53(4):2017–2039, 2015.

[48] A. Suzuki and M. Iri. Approximation of a tessellation of the plane by a Voronoĭ diagram. *Journal of the Operations Research Society of Japan*, 29(1):69–97, 1986.

[49] L. A. Vese and T. F. Chan. A multiphase level set framework for image segmentation using the mumford and shah model. *International Journal of Computer Vision*, 50(3):271 – 293, 2002. Cited by: 2249.

[50] M. Yamamoto and J. Zou. Simultaneous reconstruction of the initial temperature and heat radiative coefficient. *Inverse Problems*, 17(4):1181–1202, 2001.

[51] S. Zhu. Effective shape optimization of Laplace eigenvalue problems using domain expressions of Eulerian derivatives. *Journal of Optimization Theory and Applications*, 176(1):17–34, 2018.